

Recovery and facets for deformation twins in minerals and metals

John P. Hirth^{a,1,2,3}, Dongyue Xie^{b,c}, Greg Hirth^d, and Jian Wang^{b,2}

Contributed by John P. Hirth; received September 21, 2022; accepted January 18, 2023; reviewed by Peter Anderson and Xiaozhou Liao

Type II and IV twins with irrational twin boundaries are studied by high-resolution transmission electron microscopy in two plagioclase crystals. The twin boundaries in these and in NiTi are found to relax to form rational facets separated by disconnections. The topological model (TM), amending the classical model, is required for a precise theoretical prediction of the orientation of the Type II/IV twin plane. Theoretical predictions also are presented for types I, III, V, and VI twins. The relaxation process that forms a faceted structure entails a separate prediction from the TM. Hence, faceting provides a difficult test for the TM. Analysis of the faceting by the TM is in excellent agreement with the observations.

dislocations | disconnections | twins | phase transformations

The topological model (TM) for type I twinning has been developed and shown to agree with many observations, as summarized in refs. 1–3. The TM merges the crystallographic topological theory (4) with the physical description of a disconnection—a defect with dislocation and step character (5). The key feature is that the twinning disconnections (TDs) glide on a low-index plane and propagate the twin. The TM for the complex structures found in many minerals was presented in ref. 6 and applied for twins in plagioclase (7, 8). For low-symmetry minerals with unit cells comprising many atoms, the analysis is simplified if one considers a lattice of structural groups (6), which suffices to predict the TD properties. One must understand the shuffling of the atoms within the structural groups (6, 7) to determine the kinetics of twinning, but the detailed description of shuffling is not needed to describe the twin structure as considered here. The theoretical mechanism for type I twinning in low-symmetry crystals such as triclinic plagioclase is presented in ref. 8. For most triclinic crystals, the twin parameters deviate from those that characterize a type I twin, which motivated the definition of another twin type (type III) (9).

The types of twins are defined by the twinning elements, the planes and directions associated with the twinning shear. Instead of the historical representation of the twinning elements, K_1 and K_2 for planes, η_1 and η_2 for directions, as in refs. 10-12, we use a modified Frank notation (13) for the twinning elements; for type1/III: $k_1 = K_1$, $k_2 = K_2$, $\chi_1 = \eta_1$, and $\chi_2 = \eta_2$, and for type II/IV: $k_1 = K_2$, $k_2 = K_1$, $\chi_1 = \eta_2$, and $\chi_2 = \eta_1$ (8–14). These are useful for characterizing defects mechanistically, since k_1 is always the glide plane, but one must recall that k_1 corresponds to different planes in the classical terminology, K_1 for type I and K_2 for type II. A slight modification from refs. 14 and 15 is that we use χ instead of γ because there are already several other uses for γ in the theory. The TM for type II twinning also has been described (14–16). The focus here is on faceting of a type II or IV twin boundary. Hence, we refer much of the theoretical details of the formation of the twins to the

In many cases, the irrational type II or IV twin interfaces are close to low-index, rational planes in the matrix and twin. Faceting to such planes often occurs, driven by the reduction in surface energy but at the cost of increased local strain energy from the defects with large Burgers vectors that bound the facets. The irrational k_2 plane relaxes to a faceted structure, with rational, low-index, terrace planes separated by disconnections. Faceting is a recovery process and can be either dynamic or static. The TM is needed to precisely describe the twin interfaces that are the origins of faceted structures (7–9). In what follows, we describe: a) the mechanism of formation of type I and III twins and then of type II and IV twins; b) the mechanism of partitioning of displacements; c) definitions of twin types; d) the faceting mechanism; e) faceting in plagioclase and other crystals; and f) structures formed by static or dynamic recovery. We also propose and analyze another type of twin, type VI, analogous to types II and IV, that can form by a recovery mechanism that entails periodic lattice dislocation emission. The start of the faceting analysis is the end of the description of types I–IV twinning in ref. 9, briefly summarized here.

Significance

Twins are an important deformation mechanism in low-symmetry crystals. The TM model presented here for different types of twins supersedes the classical model and introduces specific types of twins. The twinning parameters used in constitutive modeling and in structural descriptions of twins are modified. The concepts presented here can be extended to cyclic loading, important in shape-memory alloys.

Author affiliations: ^aWashington State University, Pullman, WA 99163; ^bMechanical and Materials Engineering Department, University of Nebraska-Lincoln, Lincoln, NE 68588; ^cMaterials Physics and Applications Division -Center for Integrated Nanotechnologies (MPA-CINT), Los Alamos National Laboratory, Los Alamos, NM 87545; and ^dDepartment of Geological Sciences, Brown University, Providence, RI 02912

Author contributions: J.P.H. designed research; D.X., G.H., and J.W. performed research; J.P.H. contributed new reagents/analytic tools; D.X., G.H., and J.W. analyzed data; and J.P.H. and J.W. wrote the paper.

Reviewers: P.A., The Ohio State University; and X.L., The University of Sydney.

The authors declare no competing interest.

Copyright © 2023 the Author(s). Published by PNAS. This article is distributed under Creative Commons Attribution-NonCommercial-NoDerivatives License 4.0 (CC BY-NC-ND).

¹Present address: Green Valley, AZ 85614.

²To whom correspondence may be addressed. Email: jpmdh90@gmail.com or jianwang@unl.edu.

This article contains supporting information online at https://www.pnas.org/lookup/suppl/doi:10.1073/pnas. 2215085120/-/DCSupplemental.

Published February 16, 2023.

We present transmission electron microscope (TEM) results for two plagioclase specimens, one from an olivine gabbro with ~An₆₀ labradorite, and one from an anorthosite with An₈₃ bytownite. The oceanic gabbro was collected in Ocean Drilling Program Hole 735B. These samples of crustal gabbro formed at the Southwest Indian Ridge, experience stresses of 20 to 100 MPa during deformation at temperatures of 700 to 850 °C, and then cooled rapidly preserving the high-temperature deformation microstructures (17). The bytownite is from the lower banded series of the Stillwater intrusion (18). Some results for NiTi are also summarized. Values of characteristic parameters for these crystals are given in Supplementary Material. Lattice parameters are represented as [100], [010], [001], [α_0], [β_0], and [γ_0]. The subscripts for the angle designations are used to avoid confusion with characteristic angles in the TM.

Type I/III Precursor

As explained in ref. 9, the TDs are defined in a dichromatic pattern (DP), the superposition of the twin and matrix lattices (9). To represent the partitioning of displacements, the TDs have double Burgers vector components $2\boldsymbol{b}_g$ and a step height h. The twin displacements are defined in the plane of distortion (POD), with normal n, that contains all displacements, plane strains, and plane rotation. Orthogonal coordinates are defined by n, the normal to the twin plane, **P**, and a unit vector $Q = n \times P$, parallel to χ_1 . A portion of the 3D projection of the DP for a type III twin is shown in Fig. 1A. A key feature is that the normal to the glide plane, **P**, is nonparallel to the unit cell direction [010]; so the origins **o** and **o**', of **P** and the **t** vectors, differ. The projection of the DP along the POD normal n, is presented in Fig. 1B, showing the twin angle α . Fig. 1C is a projection along the glide plane normal for a type I twin, revealing that the *t* vectors lie in the POD for type I. For type III, in Fig. 1D, the *t* vectors do not lie in the POD, with a variation characterized by angle δ . Thus, the Burgers vector can be characterized by either $(t_T - t_M)$ or the projected t vectors in Fig. 1 C,

$$\boldsymbol{t}_{Tp} - \boldsymbol{t}_{Mp} = \boldsymbol{t}_T - \boldsymbol{t}_M \tag{1}$$

Completing the characteristic parameters, the angle between nand $[100]_M$ is β .

There is a small difference between the TM and the classical twinning model regarding α . In Fig. 1, the displacements are partitioned equally as required to satisfy the twin symmetry as described in ref. 5. Twinning breaks the crystal symmetry, but the symmetry elements, designated with a prime, are partly restored in the DP. P is a twofold axis of symmetry 2', or 2 'in some low-symmetry crystals,

$$2b = 2b \tan \alpha.$$
 [2]

In contrast, the classical (subscripts cl) theory (10–12) envisions a simple shear relation $2b_{cl} = h \tan 2\alpha_{cl}$. Since the simple (engineering) shear is $e = 2b_{cl}/h$, TD motion does not produce a simple shear e. Instead, TD motion corresponds to symmetrical simple shears b/h as in Fig. 2 (8, 13, 15). The classical model must be amended except for small values of α . It can be amended by adding a spacing defect to b_{cl} (19). The classical model is correct

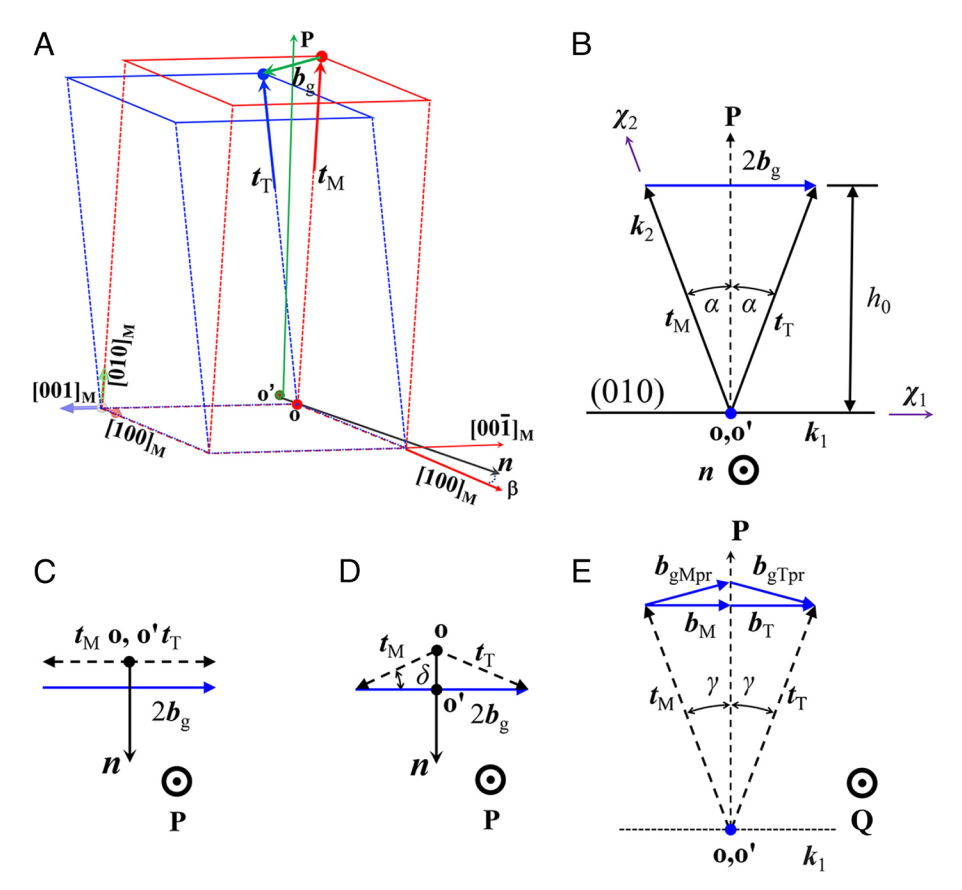


Fig. 1. (*A*) A DP for a type III twin in a generic plagioclase crystal showing $\boldsymbol{b}_g \boldsymbol{n} \boldsymbol{\beta}$, $\boldsymbol{t}_M = [010]_M$ and $\boldsymbol{t}_T = [010]_T$. The step height is $h = 2h_0$ (*B*) Projection of the DP along \boldsymbol{p} showing the (010) glide plane $k_1 \boldsymbol{P}_1 \boldsymbol{b}_g \boldsymbol{n}$, $\boldsymbol{t}_M = [010]_M$ and $\boldsymbol{t}_T = [010]_T$ for a type III twin. (*C*) Projection of the DP along \boldsymbol{P} showing that the t vectors lie in the POD for type I. (D) Projection of the DP along n showing that the t vectors lie out of the POD for type III, with the characteristic angle δ . (E) Projection along χ_1 showing angle γ . Dashed vectors throughout the paper indicate that the vectors are projected.

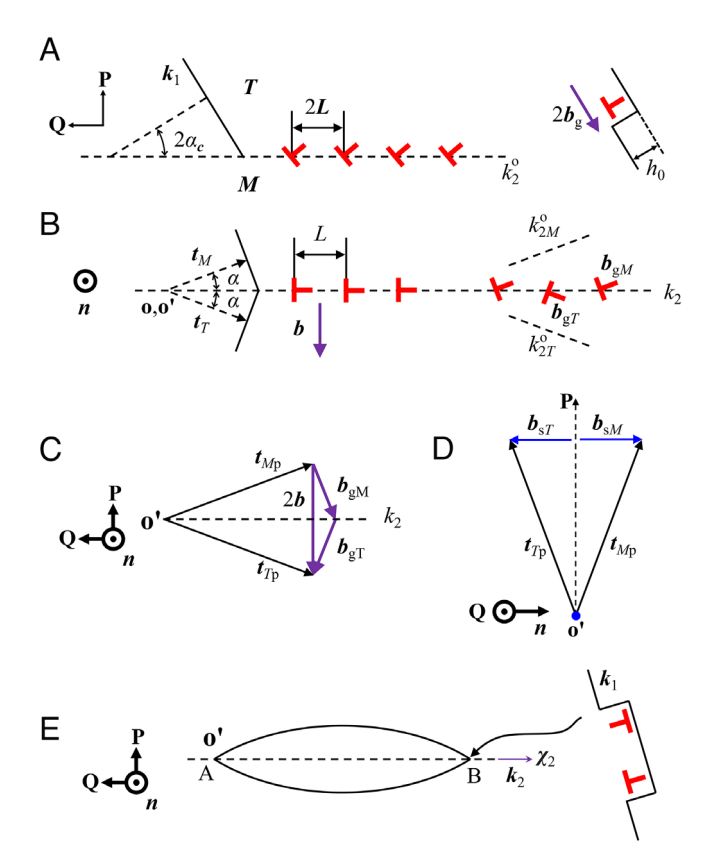


Fig. 2. (A) TDs glide on the k_1 plane and accumulate in an array on plane k_0 with elastic coherency strains. The rotation 2 α is confined to the twin. (B) The plastic distortions partition equally to the matrix and twin, removing the elastic strains. The matrix, twin, and \pmb{b}_g vectors are symmetrically rotated by α relative to the k_2 plane, which is in turn rotated by α relative to the k_0 planes. (C) Pairs of tilt dislocations in the k_2 plane have Burgers vectors equal to the vector sum of the \boldsymbol{b}_g vectors. (D) View along Q showing that the components of the t vectors are equal and opposite, so there are no screw dislocation components contributing to B. (E) The type II/IV mechanism entails pairs of TDs nucleating and propagating laterally at the tip of a lenticular twin.

for high-symmetry cases where b_g is known, e.g., $\frac{1}{6} < 112 >$ in fcc crystals. This preknowledge is not possible in low-symmetry crystals and Eq. (2) must be used.

Type II/IV Twin Interface

Twinning Mechanism. The mechanism for type II twinning entailing TD glide on a plane k_1 was suggested in ref. 14 and developed in detail in terms of the TM in refs. 15, 16, 20. A flow chart, summarizing the TM procedure (8, 16) is included in SI Appendix. The actual mechanism entails the motion of unit TDs. However, to reveal the role of symmetry we consider the hypothetical motion of double TDs followed by rotational accommodation and dissociation. The TM type II interface k_2 is rotated from the interface k_2^0 by angle α , as defined in Eq. (2). Physically, as shown in Fig. 2A, TDs glide on the k_1 plane and accumulate on the classical k_2^0 plane in an array with long-range coherency stresses. The classical, low-index twinning direction, χ_2^0 lies on the k_2^0 plane. The strains and rotations then partition equally to the matrix and twin, and the interface rotates by α . The actual twin plane, k_2 , is then rotated relative to both the twin and the matrix k_2^0 planes by α , as shown in Fig. 2B. A major consequence of partitioning is that the twinning direction χ_2 also is rotated by α from the classical value, [0 1 0] for plagioclase. The partitioned result is equivalent to having half the dislocations belonging to the twin and half to the matrix. The vector sum of these is twice

the tilt Burgers vector, $2\boldsymbol{b} = \boldsymbol{b}_M + \boldsymbol{b}_T = \boldsymbol{b}_{gM} + \boldsymbol{b}_{gT}$ as shown in Fig. 2C. The horizontal coherency components of \boldsymbol{b}_{gM} and \boldsymbol{b}_{gT} in Fig. 2D are equal and opposite and cancel, with no net contribution to \boldsymbol{b} . The screw components of \boldsymbol{b}_{gM} and \boldsymbol{b}_{gT} inclined to one another by γ as in Fig. 1E also are equal and opposite and cancel, with no net contribution to **b**.

The difference between the type I/III mechanism, where the classical model and the TM model agree except for the nonlinearity in Eq. (2) (8, 20), and the type II/IV mechanism in Fig. 2, where they do not agree, essentially arises because the former entails a single distortion mechanism, simple shear, while the latter entails two distortions, a simple shear and a rotation. After partitioning, the t vectors and α for type II/IV are the same as for type I/III. The consequence is that the partitioned k_2 plane is orthogonal to the k_1 plane. Obviously, the irrational plane cannot contain a low-index direction in triclinic crystals and other crystals, mostly low symmetry, where Q is irrational. In contrast, for example, for fcc crystals with $k_1 = (111)$, **Q** and χ_2 are parallel to < 110 >. In summary, the distinction between twin types II and IV is analogous to that between twin types I and III. If $\delta = 0$, the twin is type II. If $\delta \neq 0$, the twin is type IV (8). One additional difference is that the [100] vectors rotate out of the POD so that angle β is less than β_0 .

One limiting reference case is that for type II twins, where the **t** vectors lie in the POD, with angles α_2 , β_2 , γ_2 , and $\delta_2 = 0$. The components are the same as those in Eqs. (4-6) with the new angles inserted. Also, for a given α , b_0 is longer than \boldsymbol{b} since $\cos \delta_2 = 1$. The other limiting reference case, discussed above, is that where n lies in a low-index direction, favored when the Peierls barrier is significant or in some anisotropic elastic cases. This limit has angles α_0 , $\beta_2 = 0$, γ_0 , and δ_0 .

Partitioning Mechanism. The equipartitioning of displacements normal to a twin plane or an interphase interface is a key feature of the TM (1, 2). Such partitioning in types II/IV was introduced in refs. 9, 15, and 16. The partitioning in Fig. 1B occurs naturally, although it is easier to envision when α is small. It is analogous to partitioning at tilt walls or in phase transformations (1-3, 19). As a TD joins the tip of a growing tilt wall, the glide plane is locally bent, Fig. 3A, and the Burgers vector assumes the tilt orientation. In other words, the distortional strains naturally partition. However, the shear associated with the TD motion causes a small step with disconnection character b_d and step height h_d to form, Fig. 3B, as required by the conservation of Burgers vector law (21). These disconnections are removed by "glide", the actual mechanism for small α being a small normal shift of the tilt wall, as simulated in ref. 22. For higher tilt angles, partitioning also occurs by interface rotation, and atomistic simulation would be required to elucidate the detailed mechanism. The consequence of partitioning is a rotation of the interface by α as shown in Fig. 1. As seen in Fig. 2, the final k_2 twin plane is always inclined to k_2^0 and to both t vectors. Thus, expanding on the discussion in refs. 23 and 24, the classical description of a k_2 plane containing a low-index direction χ_2 (10-12) never applies for twins in triclinic and most other lowsymmetry crystals, and the actual χ_2 almost always is irrational. The rare exception occurs only for large α cases like fcc 111} twins. There, α is so large, 35.16°, that while the original {111} planes rotate away, new {111} planes rotate and become a k_2 twin plane with a rational χ_2 direction parallel to [112]. The classical result can be regarded as defining the reference plane k_2^0 in Fig. 1, but it always differs from the equilibrium k_2 plane. However, it always provides an approximate starting point. Hence, we defined the types of twins by the following set of conditions (9).

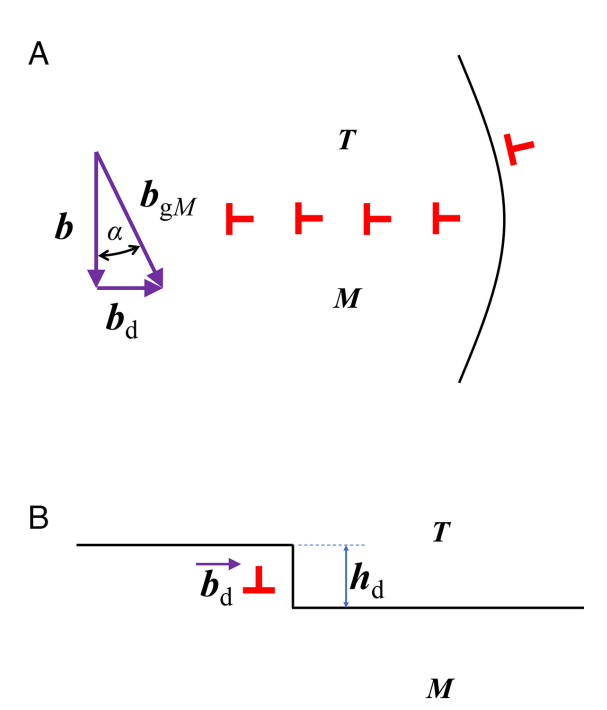


Fig. 3. (A) An example where α is small. The elastic fields of the boundary dislocations are partitioned and cause the glide plane to be curved near the boundary (25). The matrix vector \boldsymbol{b}_g splits into the tilt vector \boldsymbol{b} and a small coherency disconnection with a Burgers vector \mathbf{b}_d and a step height h = b. (B) The disconnection glides away, contributing to the interface rotation by α .

Principle 1. The twin where rational t_M and t_T vectors lie in the POD in a DP is defined as a type I twin.

Principle 2. The case where no rational t vectors lie in the POD is defined as a type III twin.

Principle 3. A type II twin is defined by the rational TD glide plane $k_1 = K_2$ and rational translation vectors \mathbf{t}_M and \mathbf{t}_T vectors in

Principle 4. A type IV twin is defined by the rational TD glide plane $k_1 = K_2$ and translation vector projections $\boldsymbol{t}_{\mathrm{Mp}}$ and $\boldsymbol{t}_{\mathrm{Tp}}$ that are irrational in the POD.

The caveat is that h must be relatively small to limit the number of shuffles (24, 26), so the rational indices must be low index. Equations for the various angles and vectors are derived in ref. 8 and are summarized in SI Appendix along with an expression for angle γ .

Facet Plane

Faceting Mechanism. In all cases of interest, the irrational type II/IV twin plane is close to a low-index plane, for example, (001) for plagioclase. Faceting entails the formation of low-index facets separated by disconnections. Faceting occurs if the decrease in surface energy is greater than the increase in strain energy associated with the disconnections. The determination of the multiple sets of dislocations for a general boundary can be complex, as discussed in ref. 21. Here, we know the line direction $\xi = n$ and the facet plane (001) that is near the twin boundary, and there is only one set of dislocations in the final interface, so the procedure is simpler. The analysis in Type II/IV Twin Interface involves double height and double Burgers vector disconnections to satisfy the partitioning symmetry. Double disconnections and dislocations are physically unstable, and the 2b dislocations would dissociate to the equilibrium arrangement of unit \boldsymbol{b} dislocations with half

the spacing as shown for the array in Fig. 4A. Initially, in the actual physical mechanism, TDs are deposited from the matrix, analogous to Fig. 2A, followed by rotational partitioning, as in Fig. 3, yielding Fig. 4B. A hypothetical equivalent would be the deposition of half the TDs from the matrix and half from the twin, automatically satisfying the partitioning, but this is physically unrealistic because the TDs must glide only in the twin to prevent profuse fault formation. The opposite sign coherency components annihilate, eliminating the local coherency strains, leaving the array in Fig. 4C with spacings L. The (001) facet plane in Fig. 4D is inclined to the type II/IV boundary by angle α as shown in Fig. 2B. Rotated relative to the (001) plane, the dislocations have mixed character, with tilt and coherency components. The dipole in Fig. 4E is composed of an array of dislocations, $-\boldsymbol{b}$, opposite in sign to those in Fig. 4D, and a disconnection with large Burgers vector, \boldsymbol{b}_D , step height h_D and separation, L_D , Here, L_D is equal and opposite to the integral Burgers vector of the boundary dislocations in the interval L_D and also has mixed character. Very near the \boldsymbol{b}_D disconnection, there are likely local pileup relaxations (27, 28), but as core-type nonlinearities, these are not considered here. Under the constraint imposed by the long-range field, the removal of the dislocations on

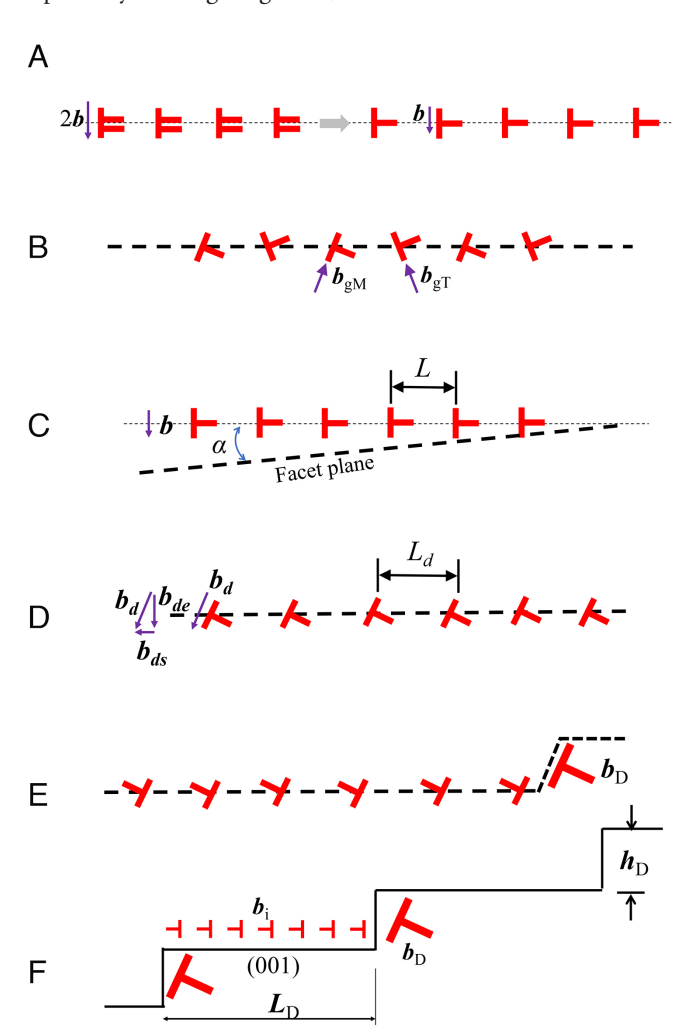


Fig. 4. (A) Double dislocations dissociate into unit dislocations. (B) Glide dislocations ${\it b}_{\rm gM}$ and ${\it b}_{\rm gM}$ resolved onto the (001) plane. (C) Equivalent representation as dislocations b after cancellation of opposite sign coherency components. (D) The dislocations are deposited onto the (001) facet plane, rotated from C, and assume mixed character in coordinates fixed on that plane. (E) Dipole of opposite sign dislocations, - b, bounded by large, like-sign disconnections, \boldsymbol{b}_D . (F) Superposition of D and E creates a (010) facet bounded by large disconnections. The facet can be represented as a continuous array of infinitesimal Bilby dislocations as shown.

the facet produces local coherency strains within a normal distance $-L_D$ from the interface according to St. Venant's principle. The equal and opposite dislocations on the facet plane annihilate when (d) and (e) are superposed. The result is shown in Fig. 4F, coherent (001) facets of spacing 2 L_D are separated by disconnections with height h_D . The steps appear because the facets are inclined to the initial twin plane. The removal of the unit defects from the facet results in local coherency strains that can be viewed as arising from a continuous array of infinitesimal Bilby dislocations (1), as indicated. The net Burgers vector is the same before and after faceting, so the longrange, strain-free rotation, 2α , is unchanged. Physically, the arrays in Fig. 4 A and B—i.e., the type II/V twins—have severe atomic overlap and, if a low-index plane is nearby, the collapse into the facet configuration should be spontaneous. For such a mechanism, there is likely a distribution of lengths with an average spacing $< L_D >$. The absolute minimum spacing $< L_D >_{min}$ is that where h_D is equal to d, the lattice spacing of (001) facet planes: otherwise, there would be a high-energy fault with misfit normal to the twin plane. In other

words, $\langle L_D \rangle_{min} = d \cot \phi$. For type I twins, TDs attract at short range and then to form disconnections with large step heights (29, 30). These steps are equivalent in structure to type II/IV twins. If large enough, they can relax by emitting lattice dislocations, converting the disconnections to pure steps. These have been observed in several metals (31) and in labradorite (7). Müllner (31), for unit disconnections, suggested that the disconnections bounding facets could be mobile on the facet plane. This would not be the case for a type II twin, but could apply if the interface was faceted because of the duality in the Burgers vector description (9). While computer simulations would be needed to specify the faceting mechanism, we postulate that the local shifting of interface sites to form a facet, once initiated, would spread spontaneously. Once the spreading is terminated, the disconnection should be sessile, with a large Burgers vector normal to the facet plane. Analogous to the type I case (29, 30), the local strain energy at a disconnection would be greatly reduced if the accumulated disconnections have a Burgers vector b_D is greater than or equal to that of a lattice dislocation, the disconnection can relax to a pure step or a disconnection with a reduced dislocation content. The strain energy is minimized when the result is a pure step, and this occurs when the step height mh_0 is that of a coincident lattice (32), or a near-coincident lattice (33), normal to the facet interface. Then, the step height and the defect spacing are increased. The linear elastic strain energy is zero when the added dislocation is the negative of the net Bilby dislocation content. Then, the pure step, equilibrium, average spacing is

$$< L_D>_{eq} = m < L_D>_{min} = md \ cot \varphi.$$
 [3]

Here *m* is an integer, and *d* is the lattice spacing normal to the facet plane. Factor m can be large, even for hcp crystals (30). In an alternate view, the Bilby content in length L is equivalent to an extended wedge disclination with strain energy associated with the singularities at the ends. The fields of these singularities are cancelled by the discrete dislocations.

Facet Characteristics. Facet formation is essentially the reverse of the partitioning from Fig. 2 A and B by a different path, so the basic DP is also the same, and n is unchanged, but angles α and γ are opposite in sign, as are the Burgers vectors. The (010) glide plane intersects the (001) plane along [100] so the as-formed facet defects have lines parallel to n_0 . The difference from the twinning case is that the twin rotates to the matrix plane (001) as shown in Fig. 5A, so that both the matrix and twin vectors rotate by the same shear. Unlike the twinning case, components that canceled for the twin

now add; so screw and coherency components appear as indicated in Fig. 5 B and C, analogous to Fig. 1E. The screw component rotation axis is P_F , with a rotation angle γ , and the line direction is \mathbf{Q}_F . The relevant final POD is (001); so the coordinates relative to this facet plane are P_F , normal to (001), \mathbf{n}_0 , and $\mathbf{Q}_F = \mathbf{n}_0 \times \mathbf{P}_F$. Physically as in Fig. 4, dislocations do not move away from the interface as parts of TDs. Instead, they are removed by locally bunching up, and the *t* vectors rotate into the interface and create a facet. Because of the stiffness of the long-range portions of the crystals, the added length in the interface is suppressed, the facets remain, but coherency strains are present. The removed dislocations of Fig. 4D are then those in the twin and the matrix that remove angles α and γ and cause the closure that creates the coherent facet. The basic angle α must be determined by the standard interrelations of the lattice parameters. We use a simpler scheme to find the other characteristics that is analytical once n and α are known. The rotation of the twin follows by symmetry. The rotations are consistent with the grain boundary theory in Chapter 19 of (21).

The diagrams relate to the double disconnections, but we present the equations for the unit dislocation component as in Fig. 4D. We first consider the limiting type IV reference case in Fig. 3F, where the normal to the POD is $n_0 = [100]$ and $b = b_0$. As in Fig. 4A, the vector \boldsymbol{b}_0 is rotated by $\boldsymbol{\alpha}$ about \boldsymbol{n}_0 , and by $\boldsymbol{\gamma}_0$ about \boldsymbol{Q}_F ; so there is an edge component normal to (010) with $\xi /\!\!/ n_0$ and length,

$$b_{en} = b_0 \cos \alpha \cos \gamma_0.$$
 [4]

There is also an edge coherency component parallel to Q_F with $\boldsymbol{\xi} \mid \boldsymbol{n}_0$ and length,

$$b_{cn} = b_0 \sin \alpha \cos \gamma_0.$$
 [5]

After the closure by α , the [010] t vectors still lie in the (100) plane inclined by γ_0 to (001). when viewed along Q_F as in Fig. 5B. Full closure is obtained by a set of screw coherency dislocations as shown in the view along with $\xi \mid |\mathbf{n}_0|$ and lengths,

$$b_s = b_0 \sin \gamma. ag{6}$$

More generally, the normal n to the POD is inclined by angle β to \mathbf{n}_0 in the glide plane. The line of such a defect can be rotated to be parallel to n_0 , and the dislocation components are then determined for this mixed dislocation with components $b \cos \beta$ and $b \sin \beta$. The portions of $b \cos \beta$ are given by Eqs. (4–6), with b replaced by $b \cos \beta$ and the subscript dropped. Thus, when $\beta \neq 0$, the normal component with $\xi \mid |\mathbf{n}_0|$ has length,

$$b_{en} = b \cos \beta \cos \alpha \cos \gamma.$$
 [7]

The edge coherency component with $\xi \mid n_0$ has length,

$$b_{cn} = b \cos \beta \sin \alpha \cos \gamma.$$
 [8]

The screw component with $\boldsymbol{\xi} \mid \boldsymbol{n}_0$ has length,

$$b_{sn} = b \cos \beta \sin \gamma.$$
 [9]

The normal component with $\xi \mid | \mathbf{n}_0$ has length,

$$b_{eQ} = b \sin \beta \cos \alpha \cos \gamma.$$
 [10]

As shown in Fig. 5C, there are two parts of $b \sin \beta$. There is a screw component $b \sin \beta$ with $\xi \mid |Q_F$. There is also an edge coherency portion – $b \cos \beta$.

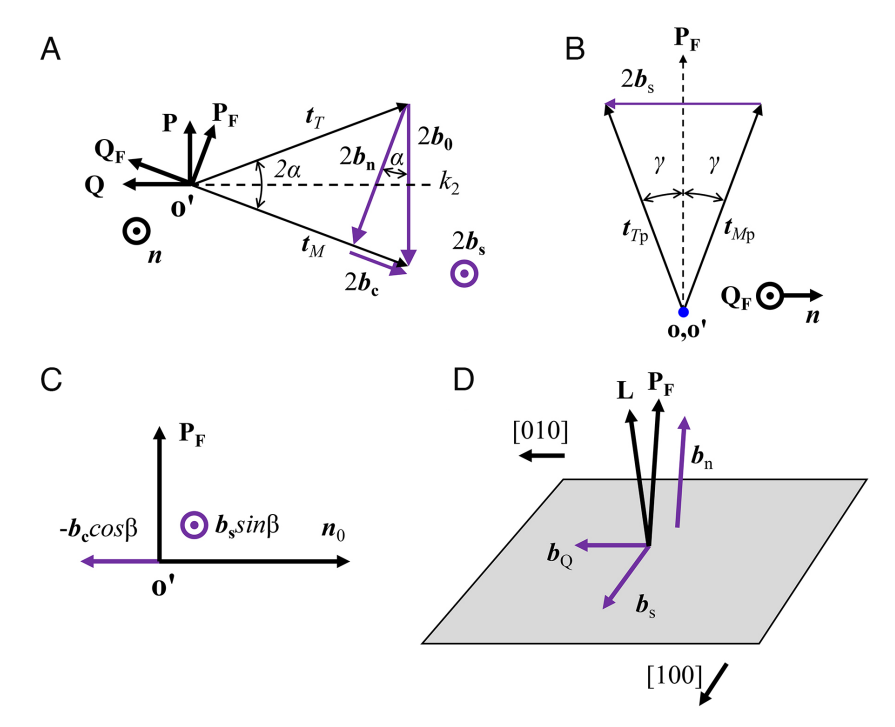


Fig. 5. (A) For the type IV case, the (001) facet plane with normal P_F is rotated by φ relative to the k_2 plane. The type IV Burgers vector $2\mathbf{b}$ has edge components $2\mathbf{b}_{en}$ normal to (001) and $2\mathbf{b}_{ec}$ parallel to (001). (B) The (010) t vectors lie in the (100) plane inclined to (001) by γ_0 , so there is also a screw component $2\mathbf{b}_s$. A view along \mathbf{Q}_F for the type IV case indicating angle γ and the screw component 2 \mathbf{b}_S . (C). View along \mathbf{Q}_F of the components of 2 b sin β . (D). Perspective view of the facet plane.

The edge coherency components with $\xi \mid Q_F$ has length

$$b_{cQ} = -b\cos\beta\sin\gamma.$$
 [11]

The screw coherency components with $\boldsymbol{\xi} \mid \boldsymbol{Q}_F$ has length

$$b_{sO} = b \sin \beta \sin \gamma.$$
 [12]

One limiting reference case is the type II case in Fig. 1*C* with angles α_{2} , β_{2} , γ_{2} , and $\delta_{2}=0$. The components are the same as those in Eqs. (4–6) with the new angles inserted. Also, for a given α , b_0 is longer than **b** since $\cos \delta_2 = 1$. The other limiting reference case, discussed above, with angles $\alpha_0, \beta_2 = 0, \gamma_0$, and δ_0 . In crystals where [010] is normal to (010), β , γ , and δ are all zero, and the equations simplify to a reduced form of Eqs. (2) and (3). This simplification is not possible for triclinic crystals, or some monoclinic and rhombohedral crystals, but is likely for higher symmetry crystals. As an example, Eqs. (5–7) apply for near monoclinic labradorite or for monoclinic NiTi, and the twins are type IV.

The structure of the interface when $\gamma = 0$ is presented in Fig. 6A, parallel arrays of disconnections with tilt, coherency, and screw components and orthogonal screw and edge coherency components, as described by the equations. When $\gamma \neq 0$, the structure is that of Fig. 6B. These figures are general in the sense that no coherent twin facet can have an extensive length for a twin terminating within a crystal, whether the twin is a type I to IV twin, a growth twin, a recovered deformation twin, or a blocky twin. Extensive twin facets/terraces only exist for twin boundaries passing completely through a crystal or terminating at a grain boundary or a defect junction. The Bilby dislocations on a facet constitute a disclination with strain sources at the terminal singularities. These must be compensated by dislocations or dislocation components of disconnections. At the jogs where the dislocation lines are displaced from one plane to the next, the dislocation character changes on the jog plane.

Disconnection Loops

As seen in Fig. 1A, for a given \boldsymbol{b}_{g} , $\boldsymbol{\beta}$ and $\boldsymbol{\delta}$ are not independent (7). With the value β_0 when $\delta = 0$ as a reference, the interrelation is

$$\delta = \beta - \beta_0.$$
 [13]

This has significance for the mesoscopic lenticular twins. TDs have a circular or elliptical shape in the glide plane. For a type I twin in plagioclase with $\delta = 0$, the Burgers vector is pure edge, $\boldsymbol{b}_{g} = \boldsymbol{b}_{ge}$, and both it and the line direction $\boldsymbol{\xi}$, parallel to \boldsymbol{n} , are irrational. If the Peierls barrier were important, the line would tend to relax to segments with $\xi = [100]$, rotated by β and separated by kinks. The screw orientation also has an irrational ξ , and would tend to form segments with $\xi = [001]$ separated by kinks but with a different rotation β_s . For the type III, $\beta = 0$ case the edge line direction would be aligned with [100] with no kinks, but because of the triclinicity, the screw line would still be inclined by β_s and would tend to form [001] segments separated by kinks. These considerations carry over to the tilt disconnection loops for either type II or IV twins. Thus, in TEM views along [100] or [001], one or the other would entail a kinked defect line.

Faceted Pericline Twins in Labradorite

Pericline twins in An (34) labradorite were studied in high-resolutiontransmission electron microscopy (HRTEM) in ref. 7. Fig. 7A shows a low-magnification view of the twin plane, and Fig. 7B shows the disconnections that separate the facets. The disconnections b_D have an average spacing $< L_D >$ of 200 nm. The step height is 5.1 nm (7). The lattice parameters and the TD and twin characteristics are presented in SI Appendix. The value of the parameter β_0 is so close to 90° that it is effectively monoclinic. There are two bounds for facets formed from type II/IV pericline twins in labradorite. Case A is type II with

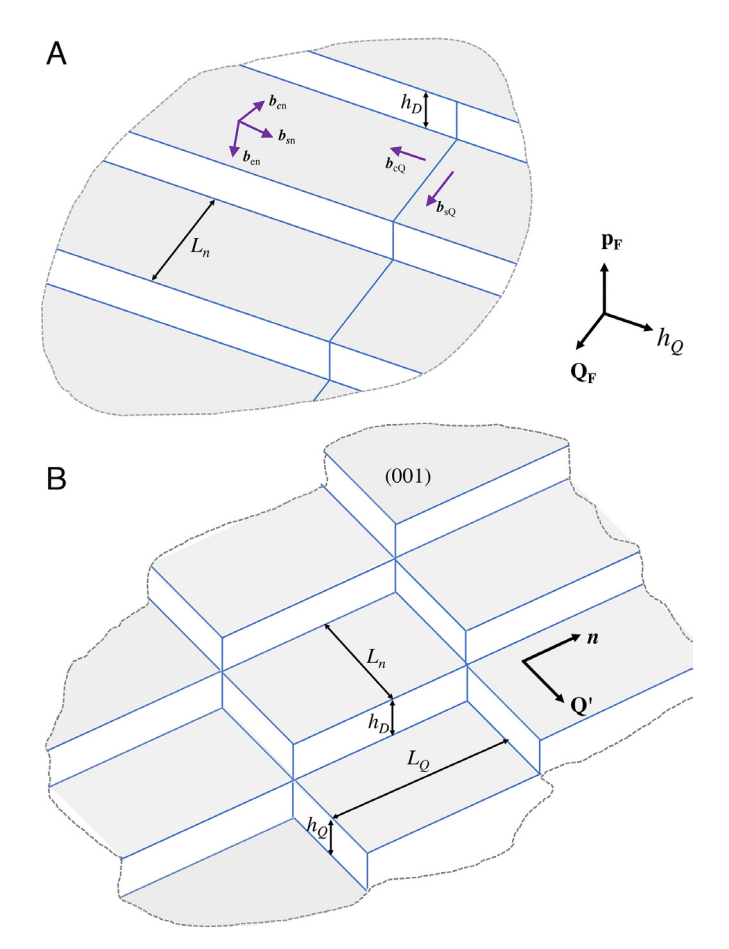


Fig. 6. (A) Perspective view of a faceted interface when $n = n_0$. (B) General case where $n \neq n_0$.

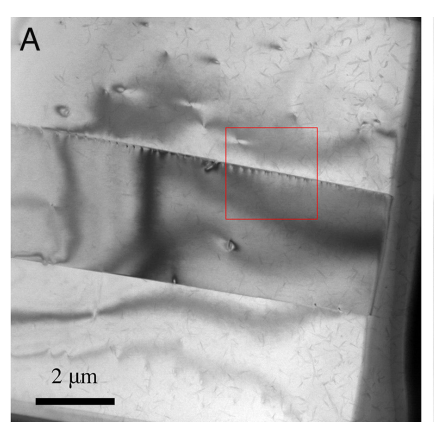
 $\alpha = 3.90$ °, $\beta = 1.117$ °, $\delta = 0$, $\gamma \cong 0$, and derived quantities $b = b_e = 0.0433$ nm, $h_d = 0.711$ nm, the spacing between (001) planes. We postulate that the minimum uniformly spaced value or minimum average value if the spacings vary, $\langle L_D \rangle_{min}$, is that where b_D the sum of the Burgers vector components normal to (001) in the interval $\langle L_D \rangle_{min}$ equals the spacing between (001) planes. For other spacings, the added dislocation content would be needed in the disconnection. Thus, there should be a tendency for uniformity in the spacings, and this appears to be the case in Fig. 4. This postulate gives < $L_D>_{min}=~16.4$ nm.Case B is type IV with $\beta = 0$, $\gamma \cong 0$, and derived quantities $\alpha = 3.90^{\circ}$,

 $b = b_e = 0.0435$ nm, $b_e = 0.0435$ °, There is a tiny screw component, but it is numerically insignificant. This gives $\langle L_D \rangle_{min} = 16.3\,$ nm. The sharp HRTEM images for labradorite (7), not the result for bytownite, imply that case B applies.

For labradorite m in Eq. (3) is 8. The m factor carries through to type IV and to the facet; so the predicted $< L_D >_{eq}$ is 130 nm. This is smaller than the observed $< L_D >$ of 200 nm. In the model, a facet is terminated when an emissary dislocation is injected, leaving a dislocation at the interface to compensate the disclination field of the facet. There is a small activation barrier for the nucleation of such a pair, associated with the core energies. Thus, one expects the length to exceed that ideal length $< L_D >_{eq}$ to provide the driving force for nucleation. This process also would account for the variation in the individual L_D values. The crystallographic rotation would be retained, and the angles would be unchanged if emissary lattice dislocations with Burgers vectors [001] were injected into the twin or matrix.

Observations of Type II/IV Twin Boundaries in **Bytownite**

Twins in deformed An80 bytownite were also characterized. A cross-polarized light micrograph is presented in Fig. 8A, in which Albite and Pericline twins can be seen. As expected, since the structure is triclinic, the twin planes are not orthogonal. An area containing a Pericline twin was extracted by focused ion beam (FIB), pasted on a copper grid, and polished to make a TEM specimen. A bright field image of the specimen is shown in Fig. 8B, where a twin lamella is seen. To identify the faceting of a Pericline twin boundary, one must accurately measure the orientation relationship between the twin and the matrix. Kikuchi patterns, sensitive to orientation change, can be collected with cameras with high dynamic range and high resolution. With the help of Kikuchi pattern simulations, the Euler angles were measured, and the angle of 2α was computed (35). For the matrix and the twin, the Kikuchi poles near the center of patterns correspond to [301] and [301], respectively. Thus, we obtained the orientation information for the twin and the matrix and demonstrated it using Euler angles with the Bunge convention. From the view of TEM images, the sample coordinate system is defined as the figure in the middle. The sample coordinate system is defined in the view of TEM images. The plane normal direction is the X-axis, the leftward direction is the Y-axis, and the upward direction is the Z-axis. Before the rotation defined by Euler angles is applied, the X-axis of the sample coordinate system is parallel to the A-axis of crystal, and the Z-axis of the sample coordinate system is



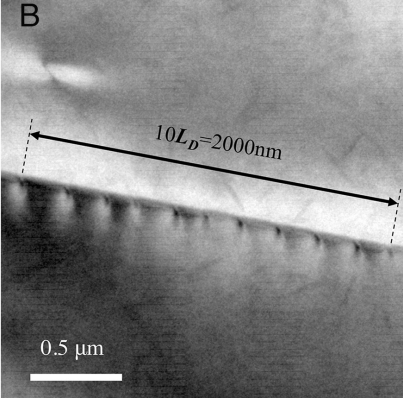


Fig. 7. TEM bright field images showing twin boundary in labradorite sample. (A) overview of the sample. (B) magnified images taken from red square in A, which shows that the average spacing of disconnections is 200 nm.

parallel to the normal direction of the c plane. The Euler angles of the matrix are 306.73°, 164.16°, and 306.86°. The Euler angles of the twin are 126.24°, 15.81°, and 52.046°. Based on this information, the misorientation angle 2α between the standard type-I twin and the observed type-II or IV twin is calculated to be 8.38° using MTEX (36). As determined by the instrument goniometer, the tilt of the respective diffraction patterns when viewed along g = [100] was $\gamma = 0.74$ between the twin and matrix. The angle between the Albite and Pericline twins in Fig. 8A is 85.3°. The model in Fig. 1 predicts a value $90^{\circ} - \alpha = 85.8^{\circ}$, a little larger. The difference arises because the surface normal must be slightly inclined relative to n so that the apparent angle is reduced from the true value.

Faceted Pericline Twins in Bytownite

The lower magnification TEM view of the twin plane, presented in Fig. 9A, reveals that the twin plane has also relaxed by faceting. The facets are separated by disconnections with an average spacing $\langle L_D \rangle$ of 550 nm. The HRTEM view in Fig. 9B is not well resolved since, as shown below, $\gamma \neq 0$. So, there are screw dislocation components to the disconnection and two separate relative rotations of the twin and matrix. Thus, a clear two-dimensional atomic resolution image could not be obtained. However, the step height of the poorly resolved disconnection, determined by counting terminating (001) planes in a view like Fig. 9B, is about 6 nm, consistent with Fig. 9A.

There are two reference bounds for facets formed from type II/ IV pericline twins in bytownite. Case A is type II with $\gamma = 0$, $\delta = 0$, $\beta_2 = 11.77^{\circ}$, $\langle L_D \rangle_{min} = 13.5$ nm, and the derived angle $\alpha_2 = 4.27$ °. This limit is obviously inconsistent with the presence of γ . Case B has the properties $\langle L_D \rangle_{min} = 13.8$ nm $\alpha_0 = 4.19^{\circ}$, $\mathbf{n} = \mathbf{n}_0$, $\delta_0 = 11.77^{\circ}$, and derived angles $\alpha_0 = 4.10^{\circ}$ and $\gamma_0 = 0.854^\circ$. The measured results are case C, close to $\beta = 0$, but the best fit is case C, with $\alpha = 4.16^\circ$, $\beta = 1.62^\circ$, $\gamma = 0.74^\circ$, $\delta = 10.1$ °, $b_{en} = 0.047$ nm, $b_{cn} = 0.018$ nm, $b_{sn} = 0.033$ nm, $b_{eQ} = 0.022$ nm, $b_{cQ} \cong 0$ nm, $b_{sQ} = 0.016$ nm, $< L_D >_{min} = 13.7$ nm, and $\langle L_F \rangle_{min} = 29.3$ nm. With these minimum lengths, the screw components would still have misfit along the defect lines. If we add the postulate that the screw components must equal the respective unit cell lengths, the results would be $< L_D >_{min} = 24.8$ nm, and $\langle L_F \rangle_{min} = 52.8$ nm. The factor m for bytownite is 10 so Eq. (3) gives $\langle L_F \rangle_{eq} = 528 \ nm$. As with labradorite, this length is smaller than the experimental value of 550 nm. The scatter in L_D values is a little larger for the bytownite case. The

explanation of both differences is the same as for labradorite. Thus, the results are in excellent agreement with the predictions in ref. 8 and show consistency between theory and measurements. The solution is close to the $\beta = 0$ limit expected for many minerals where large Peierls barriers are likely. Anisotropic elasticity could also favor the $\beta = 0$ limit. The theory and results are matched by making angle α consistent. The agreement of the theoretical and experimental values of γ provides an independent result. Thus, the TM fits all the experimental findings well.

General Facet Structure

Relation to Grain Boundary Theory. For the most general twin boundary, the displacements always have pure tilt symmetry. When the irrational k_2 boundary facets, the dislocation arrays producing the associated rotations are not restricted to single types of Burgers vectors as in the TD formation mechanisms for types I to IV twins. Because the added dislocations form an irrational array, there can be up to four sets of dislocations, two edge arrays associated with orthogonal tilts and one screw array associated with a twist, all relative to the low-index terrace. This is analogous to the reduced von Mises criterion at a grain boundary (21). If the screw arrays are orthogonal screws, they are not independent, since, operating together they produce a pure rotation without strain. However, both sets, which could be either edge or mixed in character (37) must be present to prevent coherency stresses from appearing. There are three independent systems that satisfy the compatibility condition that the \in_{xx} , \in_{yy} , and \in_{xy} strains in forming the boundary are the same in the two crystals when the axes x and y lie in the boundary, Thus, to remove any one of these sets in producing the facet, the mechanism is as follows. The atomically spaced TDs entail atom-atom overlap and should spontaneously relax, as described above, into discrete disconnections b_D bounding the low-index terraces: the facets. The net Burgers vector of the original discrete defects now resides in the disconnection as \boldsymbol{b}_{D_1} and the removal of the discrete defects leaves an array of infinitesimal Bilby coherency dislocations on the facets with a net \boldsymbol{b}_i equal and opposite to \boldsymbol{b}_D , Fig. 4F, explicitly demonstrated and simulated in ref. 1. These same considerations apply to tilt grain boundaries, to kink bands and the interfaces for shear type phase transformations when there is a large tilt component to the TDs.

Other Type IV Observations. We have focused on twins in plagioclase here, but faceted type II/IV twins are also observed in other crystals. NiTi (38-41) for example, is an example of



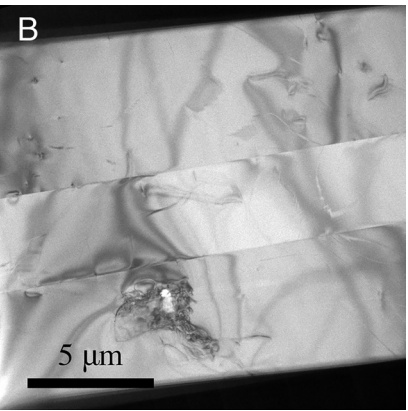


Fig. 8. (A) Cross-polarized light micrograph of deformed bytownite, showing albite and pericline twins. (B) Bright-field TEM image of deformed bytownite showing a pericline twin lamella.

a type IV twin where the measured β is intermediate between the upper and lower bounds described here. Twinning in NiTi, generally has been analyzed as type II, e.g., refs. 14, 20, 38-41. However, the analysis in ref. 7 clearly shows that the nearest t vectors, of the <110> type, do not lie in the POD: the twin is type IV, not type II. The more detailed analysis here reveals that the characteristics are as follows, including the data in refs. 37–39: $b_{en} = 0.085 \text{ nm}, b_{cn} = 0.002 \text{ nm}, b_{eQ} = 0.011 \text{ nm}, \alpha = 7,86^{\circ}, \beta = 0.002 \text{ nm}$ 7.34°. $\gamma = 0.40$ °, and $\delta = 2.73$ °, $L_e = 0.786$ nm, $L_O = 6.07$ nm. The angles are small, but are consistent with the HRTEM results in refs. 39 and 40, when viewed in the conventional [011] direction parallel to n. The major consequence of the small angle [011] direction is that the structure is that of Fig. 6B. The other boundary studied in ref. 39 can be understood only if it is a double twin boundary, possibly a result of a type IV twin nucleating during unloading at a preexisting twin boundary, formed during loading. The early HRTEM work (39, 40) clearly revealed faceting, and anticipated the type IV analysis in several ways. Thick specimens, viewed in the [011] direction close to Q_F had poor resolution because the (001) planes of twin and matrix diverged, indicating that the angle between Q_F and the [011] direction was nonzero. They also observed a structure like that in Fig. 6B, implying that the twin is type IV, and noted that spacing L_O was much greater than L_n , consistent with our calculations for bytownite. A similar twin, type IV on one side, double twinning on the other, was observed for Ni-Mn-Ga (42). The results here may be relevant to that case also.

We anticipate that facets will occur for many type II/IV twins when they are examined in HRTEM. In addition to the review of twinning elements for minerals, the partial dislocations that become components of TDs are reviewed in ref. 43. Preliminary consideration indicates that the twins in triclinic devitrite (44) are type IV twins, while those in trigonal Hg (45) are type II. Possibly, other observation of twinning modes cited as type I or II may be type III or IV when analyzed in the TM.

Recovered Twins and Large Steps

The type II/IV twins have distortion fields corresponding to those of a tilt wall, because the relative displacements of twin and matrix have mirror symmetry. This structure applies to unconstrained twins that extend to free surfaces at each end or except near the twin tips for lenticular twins with high aspect ratios. If the twins are limited in length in the direction parallel to χ_2 , there are large incompatibilities. The fields of the discrete tilt walls are equivalent to those of paired partial disclinations (46), wedge type if the step is perpendicular to the glide plane (47, 48). This field can be removed by a recovery mechanism entailing the emission of lattice dislocations into the twin or matrix, Since the net tilt vector is then nil for a completely recovered boundary, there is a change in orientation. A simple example is the type II twin in a fcc crystal. The unconstrained type II boundary has an orientation of {111}, while the recovered orientation is {112}, a rotation of 19.5°. A fully recovered blocky twin in a fcc crystal would be bounded by {111}, {112}, and {110} interfaces (29). Such blocky twins do not form in plagioclase, but they do form in metals and compounds and potentially could form in some minerals. If they do form, they would be designated as type IIR or type IVR twins to distinguish them from type II/IV twins.

Also, for type I/III twins such as Albite, large steps can form that are equivalent to Pericline twin planes. There is a short-range attraction between like-sign TDs, and if there is an obstacle, large steps occur (29, 30). The unrelaxed step heights are limited to the order of ten interplanar spacings. The fields of the steps are equivalent to those of wedge-type disclination dipoles if the step is perpendicular to the glide plane (8, 47). The defects are mixed wedge/coherency disclinations (6, 30) if the step is slanted. For a statically recovered step, the stress fields are removed by emissary dislocations ejecting into the matrix or twin. The stress-free step height $h = jh_0$ is the fixed by the condition $jb = b_D$. Results for Mg are in excellent agreement with this result (30).

Type V and VI Twins

In plagioclase where $\beta \neq 0$, no normal n, or equivalently—no line direction ξ , is parallel to a low index, rational direction for a TD. However, the Peierls stress for motion would be lower if the line direction were [100]. Anisotropic elasticity could favor such an orientation. Hence, as suggested in ref. 42 for twins in a Ni-Mn-Ga alloy, another possible faceted structure, for example for plagioclase, is that the precursor TDs that accumulate to form a boundary are mixed with \boldsymbol{b}_{gr} inclined. to [100] but with \boldsymbol{n} and $\boldsymbol{\xi}$, parallel to [100] This differs from types II or IV where the precursor TDs are pure edge, and we designate it as type VI. In other words, at the stage in Fig. 4C, the dislocations are mixed. The process carries through like that in Fig. 4, with the mixed dislocations on (001) now labeled as \boldsymbol{b}_r . The difference for type VI is that the long-range displacement field is not the rotational field of a twin but that of a twin, including the screw component of the twin field, with a superposed distortion field of a screw dislocation array with Burgers vector \boldsymbol{b}_{rs} and with both rotational and strain portions. The results resemble those for types II and IV, but the boundary is a grain boundary with mixed screw/edge dislocation character, not a twin boundary at this stage. Since the

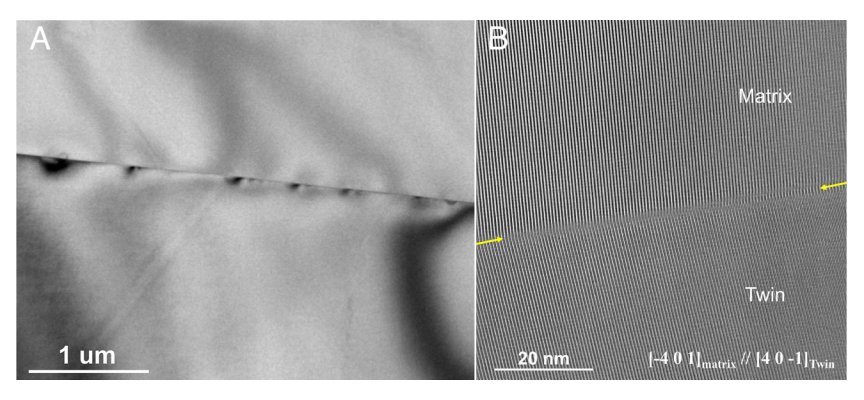


Fig. 9. (A) A bright field image of pericline twin in bytownite viewing along [401]. Twin boundary is faceted with < L_D > = 550 nm. (B) A HRTEM image of pericline twin boundary in bytownite containing a disconnection at the center.

boundary arises from glide on k_1 , we indicate the difference by designating the boundary plane as r_2 to indicate that it is distinct from a type II or IV twin boundary. A twin boundary can be created if the grain boundary undergoes a specific recovery mechanism. The mechanism can be static recovery wherein lattice screw dislocations \boldsymbol{b}_{Ls} are emitted periodically along the boundary, leaving an opposite sign screw in the boundary. More likely, the mechanism is dynamic recovery by periodic glide of such screw dislocations along with the TDs (42). The presence of the lattice screw dislocations removes the long-range screw field and results in a twin with a tilt wall with the reduced edge content $b_{re} = b_r \cos \beta$, and a corresponding reduced value of the twin angle 2α . One would need either a measurement of α or an observation of the $-\boldsymbol{b}_{Ls}$ screw to verify the model.

The latter type of mechanism (42) resembles the case where two different TDs are present for the same glide plane, which can be a type V twin. Examples are $(10\ \bar{1}\ 1)$ and $(10\ \bar{1}\ 3)$ hcp twins in Mg (49–51). Individual TDs with alternating screw character sum to give an average χ_1 with a large α . if one dominates, the overall χ_1 can deviate markedly from [1012] for $(10\bar{1}1)$, or from [3032] for (1013). A difference in the shear stress acting on the screw components suffices to give the deviating result. For $(10\ \bar{1}\ 1)$ twins such a deviation has been observed (24, 34) and is predicted in ref. 51, but is not always observed (24). This would be consistent with the screw/shear stress effect. These two hcp twins also represent one of the few examples of synchroshear. Most cited examples correspond to synchroshuffle (52). In either case, the resultant twin parameters differ from those for a type II or IV twin although the k_1 glide plane is the same.

In view of these differences, we define twins of the above form as type V and VI twins, and the type II (or IV) and VI twins become degenerate if and only if the vector [010] lies in the POD (8). This condition is not met in plagioclase, but its analog is often satisfied in high-symmetry crystals. The discussion of faceting on twins in Ni–Mn–Ga (42) suggests that the result might be a type VI twin, although the authors analyze it as type II. Double or multiple twinning are other related possibilities.

Phase Transformations

Some of the above development for shear-shuffle twinning (53) is pertinent to shear-shuffle type phase transformations, described in refs. 1-3 and 54. The TM adequately explains the common analog of type I/III transformations (2). Several modifications simplify the analysis for certain complex transformations. The use of the shifted, shifted dichromatic pattern (SDP) (6) makes the determination of shuffles easier. Another is the Crocker (55) treatment of phase transformations (and twinning) in a complex fcc-monoclinic Pu-Ga alloy. An affine monoclinic-hcp phase transformation is imposed, the defects and mechanism are determined, and the reverse affine hcp-monoclinic transformation is imposed to achieve the final structure. This method was useful in analyzing the orthorhombic-monoclinic transformation in zirconia (56). A different procedure is helpful for describing type I/III twin analogs of the phase transformations, as well as being very useful for describing the type II/IV analogs. Aside from the extension normal to the glide plane associated with a change in interplanar spacing, the transformation is exactly like that discussed here for type II/IV twins. Hence, one can use a variant of the Crocker procedure. First, impose an affine transformation to the product phase to eliminate the difference in interplanar spacing. Then, analyze the transformation as a type II/IV twin. Finally, impose the reverse affine transformation to restore the interplanar spacing. The treatment of the normal extension is the basis for the disparity between the TM and the older models. The use of this shear-shuffle-extension model could be used to amend the phenomenological mode (57–60) or that associated with the near-coincidence lattice (33). The S-S-E model could be useful for other mineral transformations, e.g., ref. 61.

Discussion

In this effort, we have concentrated on the structure of twins. Many parameters are needed in the analysis, so the description is a severe test of the TM. As such, the agreement between the TM and the TEM observations is excellent for twins in plagioclase. Hence, the amendments to the classical model are significant. We expect that the model discussed here will apply to other minerals, which tend to have both low-symmetry crystal structures and in which twinning is prevalent to satisfy the von Mises condition for plastic flow. Also, the model can apply for twinning in metals and simple compounds, which tend to have higher crystal symmetry. We mentioned type IV twins in NiTi and Ni-Ga-Mn and type V twins in hcp metals. The twins in monoclinic martensite in Pu-Ga alloys (54, 62) were analyzed by the Crocker procedure, but in ref. 63 the more accurate determination of twinning modes was done in the simplified pseudostructure. The TEM results and classical theory indicated type I twinning with $K_1 = (205)$ and $\eta_2 = [302]$. In the present context, the η_2 direction is irrational and rotated from [302] by α . The results resemble those for labradorite, but with a larger $\beta = 101.8$ °. Unlike the plagioclase twins, the twinning direction is not close to the [100] direction. Monoclinic martensite in U-Nb alloys also exhibits several types of twins (13, 64) with $\gamma_0 = 92.4$ °. The indices in these papers differ and we follow (63). The exact twins have $K_1 = (130)$ and $\eta_1 = [310]$. These were described as type I twins, which would be the case for orthorhombic U, but they are type III in martensite. The other prominent twin was described as type II, but here is type IV with $\hat{K_1} = (112)$ and K_2 irrational and approximately $(\overline{172})$. These results are consistent with the type III, IV classification. Other twins were observed less frequently and could entail interactions with the growing martensite laths. Converted to the standard mineralogical notation followed here, these indices would be

 $\beta_0=92.4^\circ$, (\$\overline{301}\$), [103} (121) and (\$\overline{721}\$), respectively. The recovery associated with facet formation implies an absence of back-stresses and hence a minimal Bauschinger effect in unloading or reverse plastic deformation. Similarly, in reverse loading, there should initially be a small reduction in yield stress. This has implications for both shape memory alloys related to NiTi (65, 66) and to minerals where type II/IV twins form. For low-strain rates, the same concepts should apply. At high strain rates, there may not be sufficient time for recovery, and both a larger Bauschinger effect and a larger reverse loading yield stress should be observed.

More generally, the same TM concepts should apply to shear–shuffle phase transformations such as the athermal or thermally activated cases for martensite, or thermally activated diffusional transformations. The TM amendments should be significant when the rotation angle α exceeds 2 or 3°.

The partitioning and symmetry apply to the plastic distortion. Any resultant elastic distortions depend on specific distortion incompatibilities. For a contained twin, all of the elastic distortion is in the twin, analogous to the Eshelby inclusion (67). For a twin between two free surfaces, the only distortion is the equipartitioned plastic rotation and there is no long-range elastic distortion. For a long, thin twin between two barriers, grain boundaries, for example, the elastic strain is localized at the ends and the plastic rotation is equipartitioned to the twin and matrix. An extended version of this case is a polysynthetic twin with thin, equal thickness twins and matrices alternating.

Emissary dislocations were mentioned above several times. If they are injected under load as a form of dynamic recovery, the Peach-Koehler force is provided by the stress field of the disclination associated with the facet, and favors injection into the twin, since as the emissary dislocation reaches the opposite side of the twin, it can compensate a disclination there. Injection into the twin has been observed in an atomistic simulation (14). The resultant dislocation loops observed in the traces of former martensite plates by HRTEM in refs. 39 and 40 may correspond to traces of the compensating disconnections.

TD motion depends upon both the parameters \boldsymbol{b} and h, and the shuffles of lattice sites as well as the atoms comprising a structural group (6) at a site (such shuffles were not addressed here). The detailed mechanism for motion can involve either kink pir nucleation over the Peierls barrier, followed by lateral kink motion; or TD bowout and breaking of pinning points. In either case, a small \boldsymbol{b} is favored. The smallest \boldsymbol{b} can be for a unit TD or one with multiple step heights as in the results for fcc metals (68, 69). Countering the trend to larger step heights, the shuffles accompanying TD motion entail diffusion-like shifts. The activation energy for motion should be lower when the number of shuffles is smaller, that is for smaller step heights. Optimization is required. A kink-pair, nucleation and growth model has been presented for several metals and alloys in the approximation that the twin is type II, and that shuffles have a minor or negligible contribution to the activation energies (70). Both assumptions are plausible for metals where α can be small and shuffles are absent or minimal. However, it would not apply to systems like plagioclase where shuffles are numerous and large (7). In ref. 70, they noted that type II twins exhibited faster growth rates for metal alloys, which was puzzling. We offer several possible explanations for such diffusion-controlled shear-shuffle mechanisms. First for the type I (or III) case, the nucleating TDs are repelled by previously emitted TDs over a relatively large distance, so there is a waiting time. In contrast, for type II (or IV), after a short growth distance emitted TDs are strongly attracted by the tilt dislocation components in the incomplete twin. Secondly, the growth distance for a unit of advance of the tilt wall is shorter. This is a very large effect if the nucleation mechanism entails a spiral source. For twins forming at near sonic speeds, such as those in zinc (71), the second effect is quite important. Also, as summarized in ref. 32, the release of elastic energy at a growing tip can augment the nucleation rate.

An important consequence of the TM model is that the direction of the Burgers vector and hence χ_2 differs from the classical model for types II and IV. This would have an effect in constitutive modeling. While we have described explicit differences from the classical model, the classical model provided the basis for the TM. The basic theory (14, 15) allows for the type III to VI twins. It is the usage of concepts related to the phenomenological model (57-60) that introduced the issues pinpointed in the TM. In particular, the elegant mathematical determination of invariant planes is in many cases inapplicable to twinning or phase transformations because partitioning is required to satisfy symmetry conditions. With a single set of TDs, only the type I and III twin planes are invariant. With dual or multiple deformation systems, invariant planes can be achieved. Examples are double twinning and Fe-C martensite containing microtwins (60). Four independent deformation systems suffice to create any possible grain boundary.

The relaxation of the twin boundaries to form facets suggests a potential way to constrain the conditions of plagioclase twinning in the crust. The samples examined here experienced relatively high-temperature conditions and cooled slowly enough to allow the facets to form. In other cases, in which transient high stresses arise associated with the propagation of earthquake ruptures near the brittle-plastic transition, in the distal regions of impact craters, or thrust sheet flexure during faulting, the temperature may be too low to allow the formation of facets. Future research could explore these possibilities.

The differences between the TM and the classical model are significant, although the models agree for type I twins unless the twinning angle α is large. For types II and IV the differences between α and the classical angle α_c are significant because the classical theory does not include partitioning. In addition, the TM definitions of types II to IV, listed in The Partitioning Mechanism, differ from the classical definitions. Although, the TM definitions are consistent with the classical, general, nonmechanistic, mathematical conditions for possible twins.

Summary

Type II and IV twins are characterized by high index, irrational twin planes. We show for two plagioclase crystals and NiTi that these planes relax by forming low index, rational facets separated by disconnections. For very large twin angles, such interfaces probably remain irrational. When the twin angle 2α is less than 10 or 15°, faceting seems likely, as observed here. For both types II and IV, the TM (1, 2) predicts that the formation mechanism entails TDs moving on a low-index plane. That suffices to enable predictions of the twin characteristics. In low-symmetry crystals such as triclinic plagioclase, there are two limiting cases. In one, the TD line direction is low index and rational, reflected here by $\beta = 0$. In the other, a low-index rational direction lies in the POD, and $\delta = 0$. Both of these and intermediate cases disagree with and extend the classical models. The present analysis indicates that the mechanism is close to the $\beta = 0$ limit but not equal to it for cases considered. Physically, this would be expected if the TDs were situated in Peierls valleys. The observed spacings of the disconnections are of the order of but exceeds the predicted average value for both labradorite and bytownite.

The type II and IV examples apply when the faceting mechanism is dynamic, occurring as the twin is formed. Added static recovery can occur by the emission of lattice dislocations.

A different mechanism, suggested in ref. 42 is shown to be analogous to that for type II/IV twins, but producing a grain-boundary. The grain boundary can relax to form a twin by static recovery, entailing the emission of lattice screw dislocations.

Data, Materials, and Software Availability. All study data are included in the article and/or *SI Appendix*.

ACKNOWLEDGMENTS. The reviewers supplied helpful comments. D.X. and J.W. acknowledge support from the US NSF (CMMI- 2132336/2132383), and TEM analysis was performed in the Nebraska Center for Materials and Nanoscience, which is supported by the NSF under Award ECCS: 1542182 and the Nebraska Research Initiative. G.H. acknowledges support from NSF: EAR-1624178. This work was performed, in part, at the Center for Integrated Nanotechnologies, an Office of Science User Facility operated for the U.S. Department of Energy (DOE) Office of Science. Los Alamos National Laboratory, an affirmative action equal opportunity employer, is managed by Triad National Security, LLC for the U.S. Department of Energy's NNSA, under contract 89233218CNA000001.

- J. P. Hirth, R. C. Pond, R. G. Hoagland, X. Y. Liu, J. Wang, Interface defects, reference spaces and the Frank-Bilby equation. Prog. Mater. Sci. 58, 749-823 (2019).
- R. C. Pond, X. Ma, Y. W. Chai, J. P. Hirth, Topological modelling of martensitic transformations Dislocat. Solids 13, 225-262 (2007).
- A. Ostapovets, A. Serra, Review of non-classical features of deformation twinning in hcp metals and their description by disconnection mechanisms. Metals 10, 1134-54 (2020).
- J. P. Hirth, Dislocations, steps and disconnections at interfaces. J. Phys. Chem. Solids. 55, 985-89
- R. C. Pond, Line defects in interfaces. Dislocat. Solids 8, 5-66 (1989).
- J. P. Hirth, J. Wang, G. Hirth, The topological model of defects and interfaces in complex structures. Am. Mineral. 104, 966–972 (2019).
- D. Y. Xie, G. Hirth, J. P. Hirth, J. Wang, Defects in deformation twins in plagioclase minerals. Phys. Chem. Minerals **46**, 959–975 (2019).
- J. P. Hirth, G. Hirth, J. Wang, Disclinations and disconnections in minerals and metals. *Proc. Natl. Acad. Sci. U.S.A.* 117, 196-204 (2020).
- J. P. Hirth, J. Wang, G. Hirth, Types III and IV deformation twins in minerals and metals. Proc. Natl. Acad. Sci. U.S.A. 119, e2118253119 (2022).
- R. W. Cahn, Plastic deformation of alpha-uranium; twinning and slip. Acta Metall. 1, 49-70 (1953).
- B. A. Bilby, A. G. Crocker, The theory of the crystallography of deformation twinning. Proc. Roy. Soc. Lond. A 288, 240-255 (1965).
- M. Bevis, A. G. Crocker, Twinning shears in lattices. Proc. Roy. Soc. Lond. A 304A, 123-134 (1968).
- F. C. Frank, Crystal dislocations-elementary concepts and definitions. Phil. Mag. 42, 809-819 13.
- J. Wang, J. P. Hirth, C. N. Tomé, Twinning nucleation mechanisms in hexagonal close-packed crystals. Acta. Mater. 57, 5521-5530 (2009).
- R. C. Pond, J. P. Hirth, Topological model of type II deformation twinning. Acta Mater. 151, 229-242 (2018)
- R. C. Pond, J. P. Hirth, K. M. Knowles, Topological model of type II deformation twinning in NiTi martensite. *Phil. Mag.* **99**, 1619–1634 (2019).
- L. Mehl, G. Hirth, Plagioclase preferred orientation in layered mylonites: Evaluation of flow laws for the lower crust. J. Geophys. Res. 113, 1-19 (2008).
- L. S. McCallum, L. D. Raedeke, E. A. Mathez, Investigations in the stillwater complex: Part I. Stratigraphy and structure of the banded zone. Amer. J. Sci. 280A, 59-87 (1980).
- R. C. Pond, J. P. Hirth, Elastic and plastic aspects of martensitic transformations. Phil. Mag. 90, 805-819 (2010).
- J. P. Hirth, J. Wang, Extension of the classical theory for types I and II twinning. J. Mater. Res. 36, 2615-2622 (2021).
- 21 P. M. Anderson, J. P. Hirth, J. Lothe, Theory of Dislocations (Cambridge University Press, Cambridge, 2017).
- H. A. Khater, A. Serra, R. C. Pond, J. P. Hirth, The disconnection mechanism of coupled migration and shear at grain boundaries. *Acta Mater.* **60**, 2007–20 (2012).
- M. Lazar, The fundamentals of non-singular dislocations in the theory of gradient elasticity: 23.
- Dislocation loops and straight dislocations. Int. J. Solids Struct. 50, 352-362 (2013). J. W. Christian, S. Mahajan, Deformation twinning. Prog. Mater. Sci. 39, 1-150 (1995). 24
- 25 J. P. Hirth, R. C. Pond, J. Lothe, Spacing defects and disconnections in grain boundaries. Acta Mater. 55, 5428-5437 (2007).
- H. A. Khater, A. Serra, R. C. Pond, Atomic shearing and shuffling accompanying the motion of twinning disconnections in zirconium. Phil. Mag. 93, 1279-1298 (2013).
- J. Wang, R. F. Zhang, C. Zhou, I. J. Beyerlein, A. Misra, Characterizing interface dislocations by atomically informed Frank-Bilby theory. J. Mater. Res. 28, 1646-1657 (2013).
- S. Shao, J. Wang, A. Misra, R. G. Hoagland, Relaxation of misfit dislocations at nodes. Mater. Sci. Forum. 783-786, 515-520 (2014).
- M. Enomoto, J. P. Hirth, Computer simulation of ledge migration under elastic interaction. Metall. Mater. Trans. 27A, 1491-150 (1996).
- M. Gong, J. P. Hirth, Y. Liu, Y. Shen, J. Wang, Interface structures and twinning mechanisms of twins in HCP metals. *Mater. Res. Lett.* **5**, 449–464 (2017). 30
- P. Müllner, Twinning stress of type I and type II deformation twins. Acta Mater. 176, 211-219 (2019)
- W. Bollmann, Crystal Defects and Crystalline interfaces (Springer-Verlag, Berlin, 1970). 32
- W. Z. Zhang, Decomposition of the transformation displacement field. Phil. Mag. 78, 913-933 (1998).
- B. Hansson, R. S. Barnes, On order twinning in AuCu Sur les macles d'ordre dans Au Cu Zwillingsbildung durch ordung in AuCu. Acta Metall. 12, 315-319 (1964).
- X.-F. Gu, T. Furuhara, W.-Z. Zhang, PTCLab: Free and open-source software for calculating phase
- transformation crystallography. *J. Appl. Cryst.* **49**, 1099–1106 (2016).

 F. Bachmann, R. Hielscher, H. Schaeben, Texture analysis with MTEX-free and open source software toolbox. Solid State Phenom. 160, 63-68 (2010).
- 37. J. P. Hirth, Stabilization of strained multilayers by thin films. J. Mater. Res. 8, 1572-1577 (1993).

- 38. K. M. Knowles, A high-resolution electron microscope study of nickel-titanium martensite. Phil. Mag A 45, 357-370 (1982).
- Z. L. Xie, Y. Liu, HRTEM study of <011> type II twins in NiTi shape memory alloy. Phil. Mag. 84, 3497-3507 (2004).
- Y. Liu, Z. L. Xie, The rational nature of Type II Twin in NiTi shape memory alloy. J. Intell. Mater. Syst. Struct. 17, 1083-1092 (2006).
- A. S. K. Mohammed, H. Sehitoglu, Modeling the interface structure of type II twin boundary in B19' NiTi from an atomistic and topological standpoint. Acta Mater. 183, 93–109 (2020).
- B. Karki, P. Müllner, R. C. Pond, Topological model of type II deformation twinning in 10M Ni-Mn-Ga. Acta Mater. 100, 604-616 (2020).
- 43. D. J. Barber, H. R. Wenk, G. Hirth, D. L. Kohlstedt, Dislocations in minerals. Dislocat. Solids 16, 171-232 (2009).
- 44. K. M. Knowles, C. N. F. Ramsey, Type II twinning in devitrite. Phil. Mag. Lett. 92, 38-48 (2012).
- D. M. M. Guyoncourt, A. G. Crocker, The deformation twinning mode of crystalline mercury. Acta Metall. 16, 529-534 (1968).
- J. C. M. Li, Disclination model of high angle grain boundaries. Surf. Sci. 31, 12-26 (1972).
- C. D. Barrett, H. El Khadiri, The role of Grain Boundary dislocations and disclinations in the nucleation of 10-12 twinning. Acta Mater. 63, 1-15 (2014).
- J. P. Hirth, R. W. Armstrong, Straight and curved disclinations and dislocation equivalents. Phil. Mag. 101, 25-37 (2021).
- A. Serra, D. J. Bacon, Computer simulation of screw dislocation interactions with twin boundaries in H.C.P. metals. Acta Metall. Mater. 453, 4465-4481 (1995).
- R. C. Pond, D. J. Bacon, A. Serra, 1995 Interfacial structure of 1011 twins and twinning dislocations in titanium. Phil. Mag. Lett. 71, 275-284 (1995).
- 51. J. Wang, I. J. Beyerlein, J. P. Hirth, C. N. Tomé, Twinning dislocations on (10-11) and (10-13) planes in hexagonal close-packed crystals. Acta Mater. 59, 3990-4001 (2011).
- M. L. Kronberg, Plastic deformation of single crystals of sapphire: Basal slip and twinning. *Acta Mater.* 5, 507–524 (1957).
- 53. R. C. Pond, J. P. Hirth, A. Serra, D. J. Bacon, Atomic displacements in deformation twinning shears and shuffle. Mater. Res. Lett. 4, 185-190 (2015).
- J. P. Hirth, R. C. Pond, Steps, dislocations and disconnections as interface defects relating to structure and phase transformations. Acta Mater. 44, 4749-4763 (1996).
- 55. A. G. Crocker, The crystallography of deformation twinning in α Plutonium. J. Nucl. Mater. 16, 306-326 (1965).
- R. C. Pond, X. Ma, J. P. Hirth, T. E. Mitchell, Disconnections in simple and complex structures. Phil. Mag. 87, 5289-5307 (2007).
- C. M. Wayman, The phenomenological theory of phase transformations: interrelationships. Metal. Mater. Trans. 25A, 1787-1795 (1994).
- M. S. Wechsler, D. S. Lieberman, T. A. Read, On the theory of the formation of martensite. Trans AIME **197**, 503-1515 (1953).
- J. S. Bowles, J. K. Mackenzie, The crystallography of martensite transformations II. Acta Metall. 2, 128-223 (1954).
- 60. M. S. Wechsler, On the theory of martensite transformations. Acta Metall. 7, 793-802 (1959).
- 61. J. P. Poirier, On the kinetics of the olivine-spinel transformation. Phys. Earth. Planet. Inter. 26, 178-187 (1981).
- 62. R. C. Pond, D. J. Bacon, A. Serra, Interfacial structure of 1011 twins and twinning dislocations in titanium. Phil. Mag. Lett. 71, 275-284 (1995).
- T. G. Zocco, M. F. Stevens, P. H. Adler, R. J. Sheldon, G. B. Olson, Crystallography of the $\delta \rightarrow \alpha$ phase transformation in a PuGa alloy. Acta Metall. Mater. 38, 2275-2282 (1990).
- R. D. Field, D. W. Brown, D. J. Thomas, Texture development and deformation mechanisms during uniaxial straining of U-Nb shape-memory alloys. Phil. Mag. 85, 2593-2609 (2005).
- D. M. Norfleet et al., Transformation induced plasticity during pseudoelastic deformation in NiOTi microcrystals. Acta Mater. 57, 3549-3561 (2009).
- H. M. Paranjape, S. Manchiraju, P. M. Anderson, A phase field-Finite element approach to model the interaction between phase transformations and plasticity in shape memory alloys. Int. J. Plasticity 80, 1-18 (2016).
- J. D. Eshelby, The determination of the elastic field of an ellipsoidal inclusion and related problems. Proc. Roy. Soc. Lond. A **241A**, 376–396 (1857).
- R. J. Kurtz, R. G. Hoagland, J. P. Hirth, Computer simulation of extrinsic grain-boundary defects in the Sigma 11, <101 > {131} symmetric tilt boundary. Phil. Mag. 79, 683-703 (1999).
- K. L. Merkle, L. J. Thompson, F. Phillipp, Thermally activated step motion observed by highresolution electron microscopy at a (113) symmetric tilt grain-boundary in aluminum. Phil. Mag. Lett. 82, 589-597 (2002).
- D. Shilo, E. Faran, B. Karki, P. Müllner, Twin boundary structure and mobility. Acta Mater. 220, 17316
- J. H. Bronton, M. P. Wilson, The kinetics of twinning in zinc and tin crystals. Proc. Roy. Soc. Lond. A 309A, 345-361 (1969).

Supplementary Materials

Recovery and facets for deformation twins in minerals and metals

John P. Hirth a,1,2, Dongyue Xie b,c, Greg Hirth d, and Jian Wang b,1

^a Private address Green Valley, Arizona 85614, U.S.A. ^b Mechanical and Materials Engineering Department, University of Nebraska-Lincoln, Lincoln, Nebraska 68588, U.S.A. ^c MPA-CINT, Los Alamos National Laboratory, Los Alamos, NM 87545, USA. ^d Department of Geological Sciences, Brown University, Providence, Rhode Island 02912, U.S.A.

¹To whom correspondence may be addressed. Email: jianwang@unl.edu or jpmdh90@gmail.com.

Contributed by John P. Hirth

A. The formation of types I-IV twins.

The key feature of the model, which involves the formation of an incipient type I twin, is shown in Figure A1(a). TDs nucleate and propagate laterally creating a type I twin. We do not consider kinetics here, although heterogeneous nucleation of a twin is almost certainly the mechanism. Heterogeneous nucleation at a grain boundary or other interface would produce half the twins. The nucleation source for the twin in Figure A1 could be some localized defect such as an inclusion or a vacancy cluster.

The initial stage of the type II twin mechanism is shown in Figure A1(b). The same TDs that produce a type I twin nucleate as pairs at the twin tip and undergo precursor glide laterally. For type II, the ratio of the nucleation rate \dot{N} to the growth rate \dot{G} is large and the twin grows faster normal to the k_1 plane than parallel to it. The interface subsequently undergoes displacement partitioning entailing rotation of the twin interface to produce the type II twin. Unlike the classical model for type II twins [10-12], the direction of twin shear is never rational in plagioclase (or other triclinic crystals), and thus a new twin, a type IV twin, is defined. The TM for such twinning is extended in [8] for the case of low-symmetry crystals, where the precursor glide is the same as the TD glide for type III twinning, as described in the previous paragraph.

² Retired.

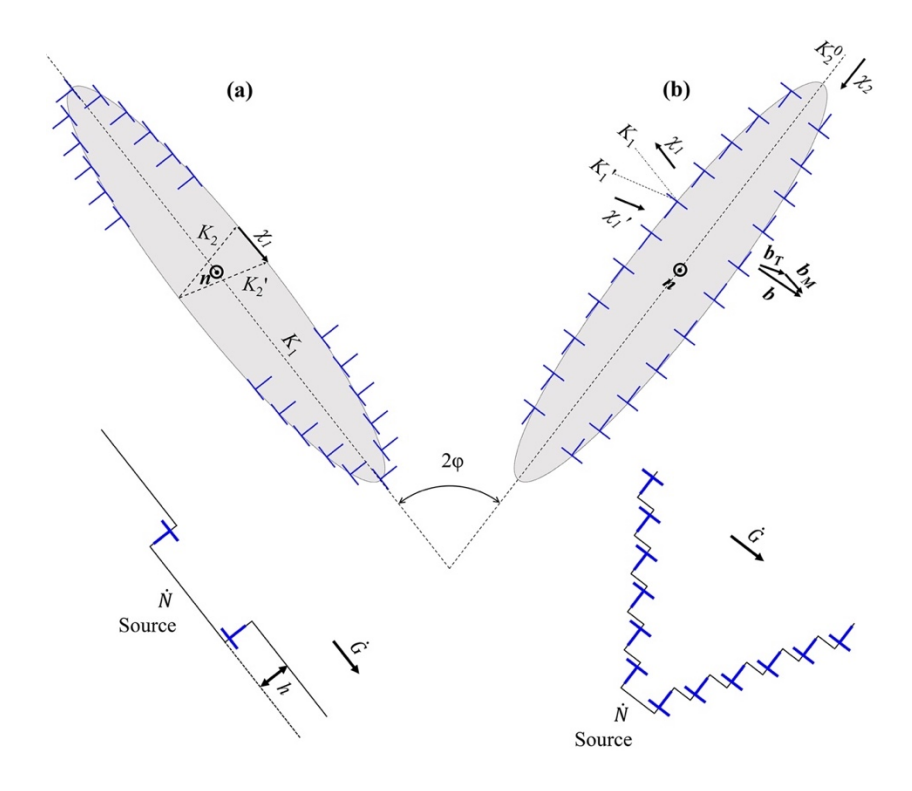


Figure. A1. Schematic illustration of the topological model for the formation of (a) type I twin and (b) type II twin in a view of the plane of distortion. Sources for the nucleation of a disconnection pair on the glide plane, k_1 , in both cases, as indicated by the inset sketches, produce the simple shear displacements. After relaxation, the k_1 planes within the type II twin are rotated by an angle α from their original orientation. The notation \hat{N} indicates a repeated nucleation site. For type I, the mobility/nucleation rate ratio \hat{G}/\hat{N} is large so the spacing L of a pair is large when a new pair nucleates at the source. For type II, the ratio is small when a new pair nucleates and interactions of the dislocation components tends to form a tilt wall, which rotates the wall by α to the final k_2 position.

The TM mechanism for a type I twin (and similarly, a type III twin) is presented in Figure A2. More relevant here, the TM mechanism for type I/III also describes the precursor glide for the creation of a type II twin (and similarly, a type IV twin). A characteristic lenticular-shaped twin is shown in Figure A2(a). Mechanistically, TD pairs nucleate and glide on the k_1 plane, as indicated at B, and propagate the type I twin or type II precursor. A TD is shown in Figure A2(b). The TDs are characterized by a Burgers vector \boldsymbol{b}_g , parallel to the twinning direction $\boldsymbol{\chi}_1$, and a step height h. For a unit TD, the step height is h_0 and for multiple heights, $h = jh_0$, with j an integer. The Burgers vector $2\boldsymbol{b}_g$ is given by the difference between lattice translation vectors \boldsymbol{t}_M and \boldsymbol{t}_T in a dichromatic pattern (DP), the superposition of the lattices of the matrix and twin with a coincident

origin on a low index dividing surface that corresponds to the twin plane. The details of the vectors are presented in a 2D projection of the DP in Figure A2(c) for a double height disconnection.

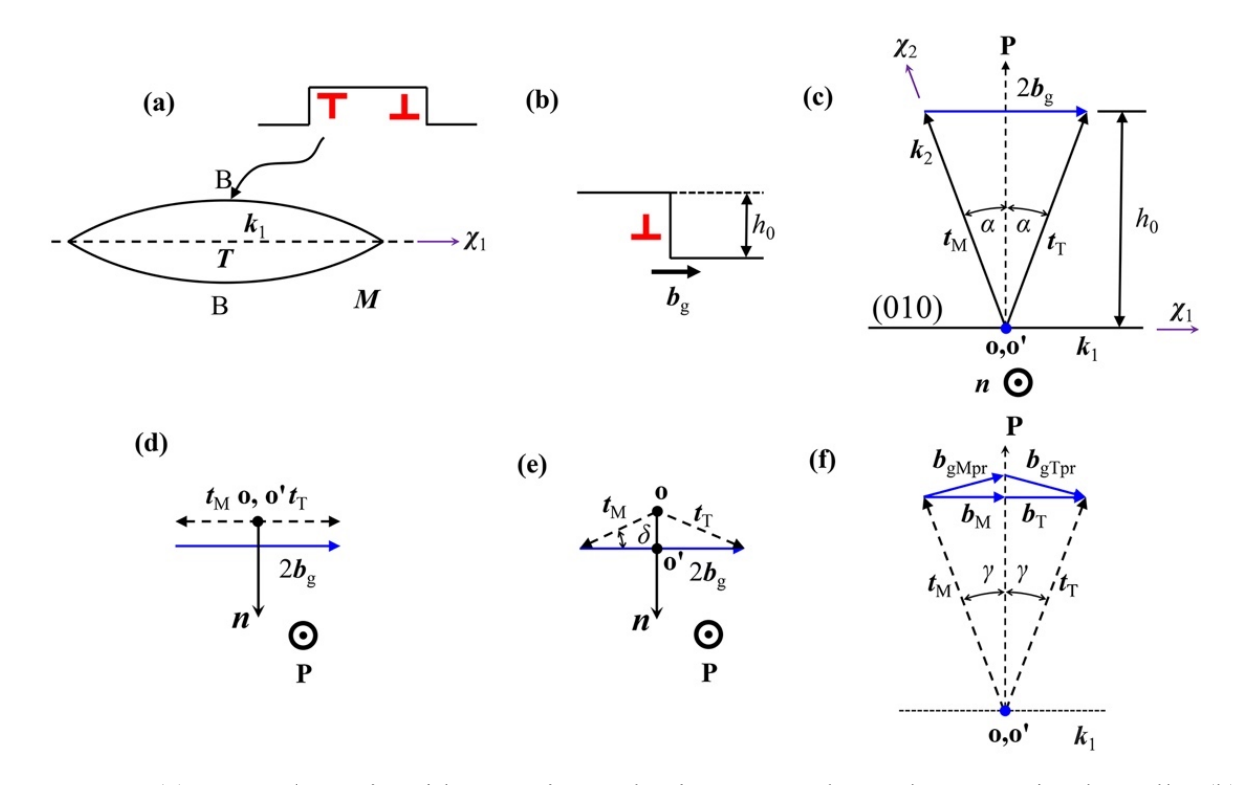


Figure A2. (a). Type I/III twin with TD pairs nucleating at A and B and propagating laterally. (b). A typical TD. For type I the t vectors are in the POD, for type III, they are projections onto the POD. (c). Portion of a three-dimensional dichromatic pattern for a generic, triclinic, plagioclase crystal, showing the (010) glide plane k_1 , b_g , n, $t_M = [010]_M$ and $t_T = [010]_T$ for a type III twin. P is the normal to (010), n is normal to the plane of distortion, and n is the Burgers vector of the TD. The n vectors and n are partitioned symmetrically to the twin n and matrix n. (d). View along the glide plane normal n of the POD showing n partitioned to the components n and n in the n glide plane for type I. (e) Analogous view for a type III twin showing the projections of the n and n vectors and the angle n of n Projection along n for type III. Dashed vectors throughout the paper indicate that the vectors are projected.

The unit vector n is normal to the plane of distortion (POD) that contains all displacements, plane strains, and plane rotations. The unit vector P is normal to the glide plane with an origin o. The unit vector $Q = n \times P$, forming an orthogonal set, is parallel to χ_1 . The sign convention for these vectors is shown in Figure A2(b). The angle β represents the difference in orientation between n and the nearest low index direction. As shown in Figure A2(c), the final twin structure is partitioned in the sense that equipartitioning of the glide vectors in the matrix and twin define

the angle 2α , a rotation that corresponds to the crystallographic two-fold axis **2** parallel to **P** and relates to the macroscopic twinning elements. For emphasis, Figure A2(c) is a view along **n**, perpendicular to both **P** and the POD and parallel to the (010) plane, which contains the vector $2\boldsymbol{b}_g$. For type I, the translation vectors lie in the POD. In contrast, for type III, the translation vectors do not lie in the POD. Thus, as illustrated, the TD vector $2\boldsymbol{b}_g$ is the closure vector defined by the translation vector components projected onto the POD, shown as dashed lines in Figure A2(c); the vector $2\boldsymbol{b}_g$ is also given by $(\boldsymbol{t}_T - \boldsymbol{t}_M)$.

$$2\boldsymbol{b}_{g} = \boldsymbol{t}_{Tp} - \boldsymbol{t}_{Mp} = \boldsymbol{t}_{T} - \boldsymbol{t}_{M} \tag{A1}$$

An important feature of the TM is indicated in Figure A2(c). For the origin o to coincide with a lattice point, the analysis always entails a double height defect as depicted here. Physically, these double-height disconnections dissociate to unit disconnections as described subsequently, giving the TD Burgers vector $\mathbf{b}_g = \frac{1}{2}(\mathbf{b}_{gM} + \mathbf{b}_{gT})$. The twin angle is given by $\sin \alpha = b_M/t_{Mp}$. Recall that for type I, the t vectors lie in the POD, as shown in Figure A2(d) for the view along P. For type III, which is the case for plagioclase, Figure A2(e) illustrates that only the components of the t vectors, rotated by $\pm \delta$ from $2\mathbf{b}_g$, are in the POD. Now P (which is normal to $2\mathbf{b}_g$) intersects the glide plane at \mathbf{o} , displaced from the unit cell point \mathbf{o} . The angle δ represents the deviation from type I: If $\delta = 0$, the twin is type I: if $\delta \neq 0$, the twin is type III. Figure A2(f) is a projection along χ_1 for type III showing that there are components of the t vectors out of the plane of distortion, defining the angle γ , although they cancel and do not contribute to the description of types I to IV twins. As shown subsequently, these out-of-plane components are important in faceting.

B. Characteristic parameters for twins in labradorite and bytownite and the TM procedure

The lattice parameters are listed in **Table 1**. The characteristic angles for the twins are defined as follows [8]:

$$\alpha = \cos^{-1}(\mathbf{t}_{\mathsf{Mp}} \bullet \mathbf{P}) / |\mathbf{t}_{\mathsf{Mp}}| \tag{B1}$$

$$\beta = \cos^{-1}(\mathbf{n} \bullet [100]) \tag{B2}$$

$$\gamma = \cos^{-1}(\boldsymbol{t}_{\mathrm{Mp}} \bullet \boldsymbol{Q}_F) / |\boldsymbol{t}_{\mathrm{Mp}}|$$
 (B3)

$$\delta = \beta - \beta_0 \tag{B4}$$

For Eq. (B1), the vector \mathbf{t}_{Mp} is resolved onto the plane normal to \mathbf{n} . For (B3), the vector \mathbf{t}_{Mp} is resolved onto the plane normal to \mathbf{Q}_F ,

$$\gamma_e = \cos^{-1}(\mathbf{t}_{\mathrm{Mp}} \bullet \mathbf{Q}_F) / |\mathbf{t}_{\mathrm{Mp}}| \tag{B5}$$

Here α_0 , β_0 , $\mathbf{n}_0 = [100]$, and b_{go} are reference values for the type II case where $\delta = 0$. The angles and \mathbf{t}_{Mp} are shown in Figures A1 and 2. In [8], \mathbf{t}_{Mp} and therefore α must be determined by the rotations described in the Supplementary Material, complex for triclinic crystals. The other angles are determined analytically. As in Figure A2(a)

$$\alpha_0 = \tan^{-1}(b_{a0}/[b_0^*] \tag{B5}$$

For plagioclase, $[b_0^*]$, parallel to **P**, is the reciprocal lattice vector. As in Figure 3(c),

$$\alpha = tan^{-1}(b_g/[b_0^*],)$$
 (B6)

Since $b_g = b_{g0} \sec \delta$,

$$\alpha = tan^{-1}(\tan \alpha_0 \sec \delta) \tag{B7}$$

The angles α and γ are not independent. From Figures 1 and 3,

$$an \gamma = \tan \alpha \tan \delta \tag{B8}$$

The angles and other characteristic parameters are listed for labradorite and bytownite in Tables 2 and 3 for two special cases that likely are upper and lower bounds for β : case A with $\beta = 0$ and case B with $\delta = 0$.

Table 1. Lattice parameters of plagioclase.

Component/Name			Lattice parameters							
		$a_0(nm)$	$b_0(nm)$	$c_0(nm)$	$\alpha_0(^\circ)$	β ₀ (°)	γ ₀ (°)			
An52	Labradorite	0.818	1.286	0.711	93.530	116.210	89.920			
An85	Bytownite	0.819	1.288	0.710	93.370	116.040	90.870			

Table 2. Properties of type I and II twins in plagioclase.

Component	K_{I}	x_1	K_2	<i>x</i> ₂	n	2α (°)	β(°)	δ(°)	$h_0(nm)$	2 bg (nm)
An52	(010)	[0.050 0 0.137]	(-1 0 38.333)	[010]	[1 0 0.026]	7.80	1.18	0	0.642	0.087
An85	(010)	[0.080 0 0.147]	(1 0 3.356)	[010]	[1 0 -0.298]	8.54	11.77	0	0.642	0.096

Table 3. Properties of type III/IV twins in plagioclase (special case with $\beta = 0$).

Component	K_{I}	x_I	K_2	x_2	n	2α(°)	β(°)	δ(°)	$h_0(nm)$	2 bg (nm)
An52	(010)	[0.053,0,0.137]	(001)	[-0.002,1,0]	[1 0 0]	7.79	0	1.18	0.642	0.087
An85	(010)	[0.056,0,0.147]	(001)	[0.024,1,0]	[1 0 0]	8.36	0	11.77	0.642	0.094

The relevant TM procedure used in the present calculations [8, 16] is as follows. One needs some experimental input, either the twinning angle α or the Burgers vector \boldsymbol{b}_g , and the glide plane

 k_1 . This is sufficient to create a dichromatic pattern like that in Fig. 1(a). For a type I plane, Eq. (2) applies, the t vectors are known and the solution is complete. The same is true for type III but one must also deduce either the screw component of \boldsymbol{b}_g or the angle γ . For type II, \boldsymbol{b}_g must be parallel to [001], $\delta = 0$, and α is then specified. As in Figure 3, this is a limiting case of type IV. For both labradorite and bytownite, α adiffers from the type II value and the twin is type IV. For type IV, the procedure followed here is more complicated. Values of α are tabulated in [8] for a range of δ values. The procedure is then to determine which value of δ provides a match to the experimental value of α . All of the other quantities above are known. As reported, for both minerals the value of δ in intermediate between the two limiting values. As an added check for bytownite, the experimental value for γ matches the calculated value.

C. Selection of step height and complementary Burgers vectors.

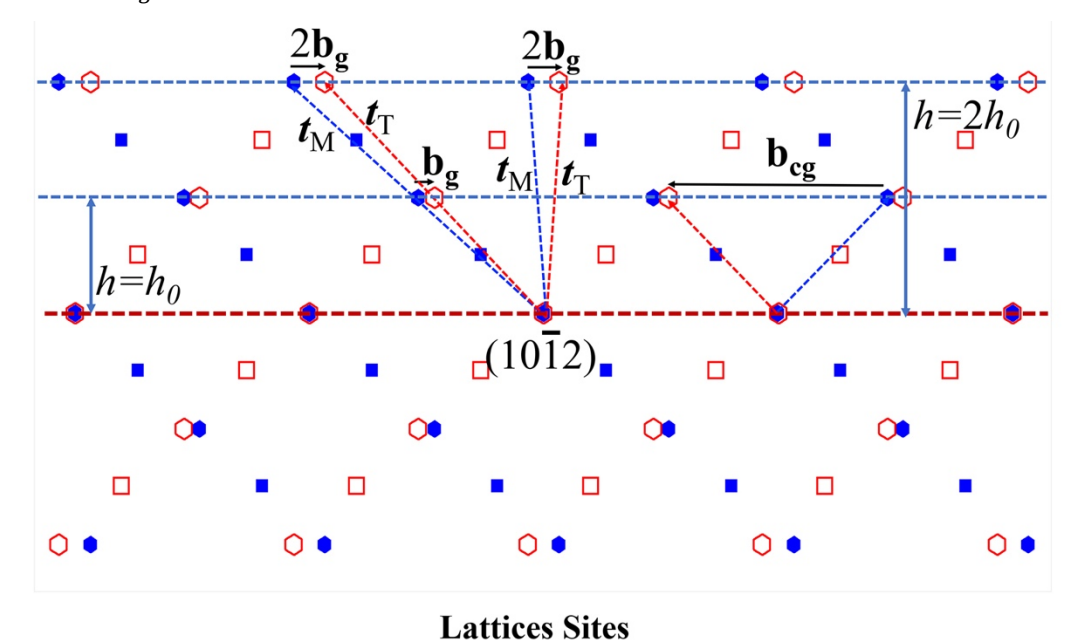
In the text, we mention the selection of \boldsymbol{b} and h. An example with many choices is the $\Sigma 11$ (001) twin in fcc crystals [70]. The favored choice theoretically was $h=4h_0$ because of its small Burgers vector and this agreed with experimental observation [71]. Another aspect is that there are symmetry related limitations on α [1,74,75] For the $\Sigma 11$ twin, the upper limit is 45°. For larger angles, a different [100] variant with an angle reduced by 45° is selected. For a given DP there is a dichotomy in the choice of \boldsymbol{b}_g when there is 2D coincidence of a boundary as for coherent twin planes [2, 10] and some grain boundaries. If the repeat distance parallel to \boldsymbol{b}_g is \boldsymbol{a} , then the same twin can be created by an opposite sign complementary dislocation $-\boldsymbol{b}_{Cg}$, where, for the same h

$$\boldsymbol{b}_g + \boldsymbol{b}_{Cg} = \boldsymbol{a} \tag{C1}$$

Thus, there is another limit. For the $\Sigma 11$ case \boldsymbol{b}_g is the appropriate choice when $\alpha < 22.5^\circ$, but for larger angles \boldsymbol{b}_{cg} is appropriate. Hence the limit for α is \pm 22.5°.

For type I twins or type II precursors with the same h, both vectors have the same rational origin for the related t vectors, and both have an associated but different twin angle α or α_C , in accord with the 2', m' symmetry, so the choice between them is obvious. An issue arises when there are different step heights. An example is Figure C1. For $h = 2h_0$, the t vectors are symmetric, the origin is rational b_g is small, and b_{Cg} is large. The choice of b_g is obvious. For $h = h_0$, b_g is large and b_{Cg} is the appropriate TD vector. However, the symmetric origin for b_{Cg} is irrational

and would greatly complicate the TM analysis. Hence, while the unit TDs have Burgers vectors $\mathbf{b}_{cq} = (1/2) 2\mathbf{b}_q$, $h = 2h_0$ is selected for analysis.



□ A-Plane in twin ○ B-Plane in twin • A-Plane in matrix • B-Plane in matrix

Figure C1. The DP for a type I hcp (10-12) twin with $\boldsymbol{b}_g = \frac{1}{2} [10\overline{1}1]$.

D. Determination of crystallographic quantities of twinning elements.

For a triclinic lattice, the unit cell is described by three base vectors \mathbf{a}_0 , \mathbf{b}_0 and \mathbf{c}_0 , and the angles α_0 , β_0 , and γ_0 between \mathbf{b}_0 and \mathbf{c}_0 , \mathbf{c}_0 and \mathbf{a}_0 , \mathbf{a}_0 and \mathbf{b}_0 , respectively. Since the three base vectors are non-orthogonal, all vector operations must be transformed to Cartesian coordinates, and then back to crystal coordinates.

D.1 Conversion between crystal direction and vectors in Cartesian coordinates

In the Cartesian coordinate system, a_0 is the magnitude of \mathbf{a}_0 in the positive x-axis direction, b_0 is a positive y-axis component of the \mathbf{b}_0 , and \mathbf{c}_0 is the positive z-axis component of the \mathbf{c}_0 . With these conditions, the basis vectors \mathbf{a}_i of the Cartesian coordinate system are expressed by the following equations.

$$\mathbf{a_1} = (a_0, 0, 0)$$

$$\mathbf{a_2} = (b_0 \cos(\gamma_0), b_0 \sin(\gamma_0), 0)$$

$$\mathbf{a_3} = (c_x, c_y, c_z)$$
(D1)

where,

$$c_{x} = c_{0} cos(\beta_{0})$$

$$\begin{split} c_y &= c_0 \frac{\cos(\alpha_0) - \cos(\gamma_0) \cos(\beta_0)}{\sin(\gamma_0)} \\ c_z &= \frac{\Omega}{a_0 b_0 \sin(\gamma_0)} \\ \Omega &= a_0 b_0 c_0 \sqrt{1 - \cos^2{(\alpha_0)} - \cos^2{(\beta_0)} - \cos^2{(\gamma_0)} + 2\cos{(\alpha_0)} \cos{(\beta_0)} \cos{(\gamma_0)}} \end{split}$$

 Ω is the volume of a unit cell. The indices in the crystal coordinate system [uvw] are converted to a vector in Cartesian coordinates by the following expression. A is the transformation matrix between crystal coordinate and Cartesian coordinates.

$$[xyz] = [uvw] \begin{bmatrix} a_1 \\ a_2 \\ a_3 \end{bmatrix} = [uvw]A$$
 (D3)

$$[xyz] = [uvw] \begin{bmatrix} a_1 \\ a_2 \\ a_3 \end{bmatrix} = [uvw]A$$

$$A = \begin{bmatrix} a_0 & 0 & 0 \\ b_0 \cos(\gamma_0) & b_0 \sin(\gamma_0) & 0 \\ c_0 \cos(\beta_0) & \frac{c_0 (\cos(\alpha_0) - \cos(\beta_0) \cos(\gamma_0))}{\sin(\gamma_0)} & \frac{\Omega}{a_0 b_0 \sin(\gamma_0)} \end{bmatrix}$$
(D4)

D.2 Conversion between Miller indices and plane normal in Cartesian coordinates

Similarly, the indices of crystal planes (Miller indices) and normal vector of a plane are related by reciprocal lattice vectors **b**. The reciprocal lattice vectors are determined from the basis vectors in Cartesian coordinates in real space.

$$\mathbf{c}_{1} = \frac{\mathbf{a}_{2} \times \mathbf{a}_{3}}{\mathbf{a}_{1} \cdot (\mathbf{a}_{2} \times \mathbf{a}_{3})}$$

$$\mathbf{c}_{2} = \frac{\mathbf{a}_{3} \times \mathbf{a}_{1}}{\mathbf{a}_{2} \cdot (\mathbf{a}_{3} \times \mathbf{a}_{1})}$$

$$\mathbf{c}_{3} = \frac{\mathbf{a}_{1} \times \mathbf{a}_{2}}{\mathbf{a}_{3} \cdot (\mathbf{a}_{1} \times \mathbf{a}_{2})}$$
(D5)

The normal vector [xyz] of a plane can be related to the index of this plane (hkl) by the following equation. Therefore, B is the transformation matrix between the Miller index of a plane and its normal.

$$[xyz] = [hkl] \begin{bmatrix} \mathbf{c}_1 \\ \mathbf{c}_2 \\ \mathbf{c}_3 \end{bmatrix} = [hkl]B$$
 (D6)

$$B = \begin{bmatrix} \frac{1}{a_0} & -\frac{\cos(\gamma_0)}{a_0 \sin(\gamma_0)} & -\frac{b_0 c_0 (\cos(\beta_0) - \cos(\alpha_0) \cos(\gamma_0))}{\sin(\gamma_0) \Omega} \\ 0 & \frac{1}{b_0 \sin(\gamma_0)} & -\frac{a_0 c_0 (\cos(\alpha_0) - \cos(\beta_0) \cos(\gamma_0))}{\sin(\gamma_0) \Omega} \\ 0 & 0 & \frac{a_0 b_0 \sin(\gamma_0)}{\Omega} \end{bmatrix}$$
(D7)

D.3 Rotation matrix associated with twinning

The orientation relationship between twin and matrix is related by the rotation around a specific axis. The rotation matrix R for a rotation around axis $u = (u_x, u_y, u_z)$ by an angle θ is:

$$R(u, \theta) =$$

$$\begin{bmatrix} \cos\theta + u_x^2(1-\cos\theta) & u_xu_y(1-\cos\theta) - u_z\sin\theta & u_xu_z(1-\cos\theta) + u_y\sin\theta \\ u_yu_x(1-\cos\theta) + u_z\sin\theta & \cos\theta + u_y^2(1-\cos\theta) & u_yu_z(1-\cos\theta) - u_x\sin\theta \\ u_zu_x(1-\cos\theta) - u_y\sin\theta & u_zu_y(1-\cos\theta) + u_x\sin\theta & \cos\theta + u_z^2(1-\cos\theta) \end{bmatrix} (D8)$$

By applying the matrix on the vector [xyz], one can obtain the rotated vector [$x_ry_rz_r$].

$$[x_r y_r z_r] = [xyz]R(u, \theta)$$
(D9)

This rotation matrix can be applied to the basis vectors, so that a crystal direction in the twin can be transformed into one in the matrix. For example, a crystal direction $[uvw]_T$ in the twin can be converted to a crystal direction in the matrix, $[uvw]_M$.

$$[uvw]_{M} = [uvw]_{T}(AR_{T})(AR_{M})^{-1}$$
(D10)

 R_T and R_M are the rotation matrices imposed on the twin and the matrix, respectively. In this equation, the crystal direction [uvw]_T was converted to a vector in Cartesian coordinates by (AR_T) and transformed to crystal direction in matrix by (AR_M)⁻¹. In a similar way, the cross product can be calculated in Cartesian coordinates and converted to fractional coordinates.

D.4 Calculation of angles

i) The angle θ between two vectors $[u_1v_1w_1]$ and $[u_2v_2w_2]$ is

$$\theta = \arccos\left(\left(u_1 \, u_2 \, a_0^2 + v_1 \, v_2 \, b_0^2 + w_1 \, w_2 \, c_0^2 + \cos(\gamma_0) \left(u_1 \, v_2 + u_2 \, v_1\right) a_0 \, b_0 + \cos(\beta_0) \left(u_1 \, w_2 + u_2 \, w_1\right) a_0 \, c_0 + \cos(\alpha_0) \left(v_1 \, w_2 + v_2 \, w_1\right) b_0 \, c_0\right) / I_{u_1 v_1 w_1} I_{u_2 v_2 w_2}\right) \quad (D11)$$

where $I_{uvw} =$

$$\sqrt{{a_0}^2\,{u}^2 + {b_0}^2\,{v}^2 + {c_0}^2\,{w}^2 + 2\,\cos(\gamma_0)\,\,a_0\,\,b_0\,\,u\,v + 2\cos(\beta_0)\,a_0\,c_0\,u\,w + 2\cos(\alpha_0)\,b_0\,c_0\,v\,w}$$

ii) The angle θ between two crystal planes $(h_1k_1l_1)$ and $(h_2k_2l_2)$ is

$$\theta = \arccos\left(d_1 d_2 \left(\frac{S_{12} (h_1 k_2 + h_2 k_1) + S_{13} (h_1 l_2 + h_2 l_1)}{+S_{23} (k_1 l_2 + k_2 l_1) + S_{11} h_1 h_2 + S_{22} k_1 k_2 + S_{33} l_1 l_2} \right) / \Omega^2 \right)$$
(D12)

where
$$\frac{1}{d^2} = (S_{11} h^2 + S_{22} k^2 + S_{33} l^2 + 2 S_{12} h k + 2 S_{13} h l + 2 S_{23} k l)/\Omega^2$$
.

$$S_{11} = b_0^2 c_0^2 \sin(\alpha_0)^2$$

$$\begin{split} S_{22} &= a_0^2 c_0^2 \sin(\beta_0)^2 \\ S_{33} &= a_0^2 b_0^2 \sin(\gamma_0)^2 \\ S_{12} &= a_0 b_0 c_0^2 (\cos(\alpha_0) \cos(\beta_0) - \cos(\gamma_0)) \\ S_{23} &= a_0^2 b_0 c_0 (\cos(\alpha_0) \cos(\beta_0) - \cos(\gamma_0)) \\ S_{13} &= a_0 b_0^2 c_0 (\cos(\alpha_0) \cos(\beta_0) - \cos(\gamma_0)) \end{split}$$

The angle θ between two crystal directions $[u_1v_1w_1]$ and $[u_2v_2w_2]$ can be expressed by

$$\theta = \arccos \left(\left(([u_1 v_1 w_1] A) \cdot ([u_2 v_2 w_2] A) \right) / (|[u_1 v_1 w_1] A| \cdot |[u_2 v_2 w_2] A|) \right) \tag{D13}$$

iii) For the angle between two planes or between a direction and a plane, the matrix B is substituted for matrix A.